Tumor-associated high endothelial venules mediate lymphocyte entry into tumors and predict response to PD-1 plus CTLA-4 combination immunotherapy

Assia Asrir, Claire Tardiveau, Juliette Coudert, Robin Laffont, Lucas Blanchard, Elisabeth Bellard, Krystle Veerman, Sarah Bettini, Fanny Lafouresse, Estefania Vina, et al.

Cancer Cell

Article

Tumor-associated high endothelial venules mediate lymphocyte entry into tumors and predict response to PD-1 plus CTLA-4 combination immunotherapy

Graphical abstract

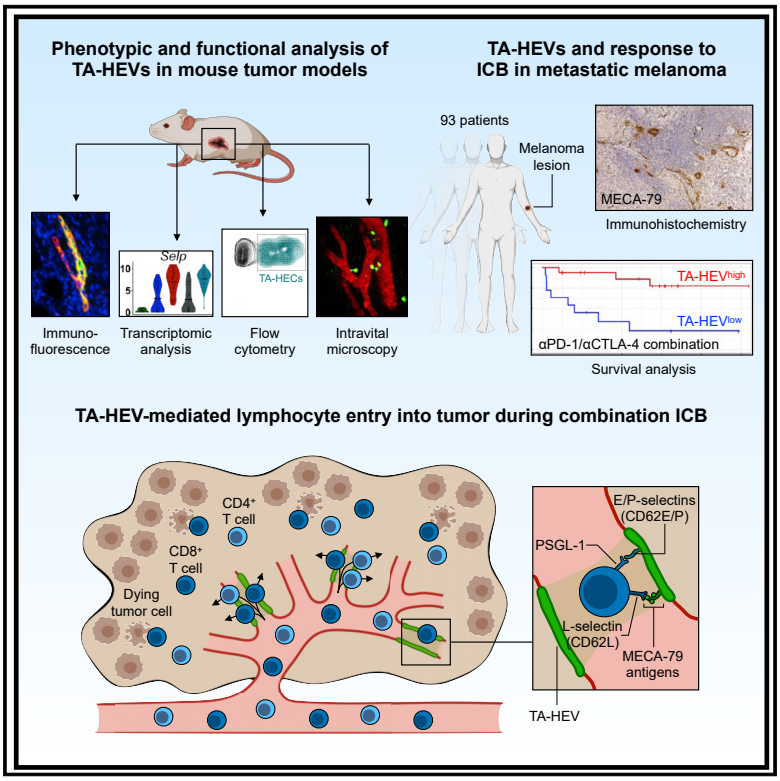

Highlights

- TA-HEVs are main sites of lymphocyte extravasation into αPD-1/αCTLA-4-treated tumors
- TA-HEV endothelial cells (TA-HECs) have a unique bifunctional hybrid phenotype
- Increasing TA-HEC differentiation increases the proportion of stem-like CD8$^+$ T cells
- TA-HEVs predict response and survival of melanoma patients treated with αPD-1/αCTLA-4

Authors

Assia Asrir, Claire Tardiveau, Juliette Coudert, ..., Nathalie Ortega, Caroline Robert, Jean-Philippe Girard

Correspondence

jean-philippe.girard@ipbs.fr

In brief

Asrir et al. show that specialized blood vessels designated tumor-associated HEVs (TA-HEVs) function as major sites of lymphocyte entry into tumors during cancer immune response and immunotherapy. Consistently, high numbers of TA-HEVs in melanoma lesions are associated with better clinical response and survival of patients treated with αPD-1/αCTLA-4 combination.

Asrir et al., 2022, Cancer Cell *40*, 1–17
March 14, 2022
https://doi.org/10.1016/j.ccell.2022.01.002

CellPress

Cancer Cell

CellPress
OPEN ACCESS

Article

Tumor-associated high endothelial venules mediate lymphocyte entry into tumors and predict response to PD-1 plus CTLA-4 combination immunotherapy

Assia Asrir,[1,9] Claire Tardiveau,[1,9] Juliette Coudert,[1,9] Robin Laffont,[1,9] Lucas Blanchard,[1,9] Elisabeth Bellard,[1] Krystle Veerman,[1] Sarah Bettini,[1] Fanny Lafouresse,[1] Estefania Vina,[1] Dorian Tarroux,[1] Severine Roy,[2,3] Isabelle Girault,[2,3] Irma Molinaro,[4] Frédéric Martins,[5,6] Jean-Yves Scoazec,[3,4,7,8] Nathalie Ortega,[1] Caroline Robert,[2,3,7] and Jean-Philippe Girard[1,10,*]

[1]Institut de Pharmacologie et de Biologie Structurale, IPBS, Université de Toulouse, CNRS, UPS, Toulouse, France
[2]Department of Medicine, Gustave Roussy, Villejuif, France
[3]INSERM U981, Gustave Roussy, Villejuif, France
[4]Department of Pathology, Gustave Roussy, Villejuif, France
[5]Institut des Maladies Métaboliques et Cardiovasculaires, I2MC, UMR1048, INSERM, UPS, Toulouse, France
[6]Plateforme Genome et Transcriptome, GeT, Genopole Toulouse, France
[7]Paris-Saclay University, Orsay, France
[8]AMMICa, CNRS-UAR 3655 and INSERM-US23, Gustave Roussy, Villejuif, France
[9]These authors contributed equally
[10]Lead contact
*Correspondence: jean-philippe.girard@ipbs.fr
https://doi.org/10.1016/j.ccell.2022.01.002

SUMMARY

Recruitment of lymphocytes into tumors is critical for anti-tumor immunity and efficacious immunotherapy. We show in murine models that tumor-associated high endothelial venules (TA-HEVs) are major sites of lymphocyte entry into tumors at baseline and upon treatment with anti-PD-1/anti-CTLA-4 immune checkpoint blockade (ICB). TA-HEV endothelial cells (TA-HECs) derive from post-capillary venules, co-express MECA-79$^+$ HEV sialomucins and E/P-selectins, and are associated with homing and infiltration into tumors of various T cell subsets. Intravital microscopy further shows that TA-HEVs are the main sites of lymphocyte arrest and extravasation into ICB-treated tumors. Increasing TA-HEC frequency and maturation increases the proportion of tumor-infiltrating stem-like CD8$^+$ T cells, and ameliorates ICB efficacy. Analysis of tumor biopsies from 93 patients with metastatic melanoma reveals that TA-HEVs are predictive of better response and survival upon treatment with anti-PD-1/anti-CTLA-4 combination. These studies provide critical insights into the mechanisms governing lymphocyte trafficking in cancer immunity and immunotherapy.

INTRODUCTION

Immune checkpoint blockade (ICB) therapy with anti-PD-1 (nivolumab) and/or anti-CTLA-4 (ipilimumab) antibodies provides therapeutic benefit for many patients across different types of cancer (Ribas and Wolchok, 2018; Sharma et al., 2021). Anti-PD-1 and anti-CTLA-4 antibodies utilize different cellular mechanisms, and targeting both pathways leads to increased anti-tumor responses (Gide et al., 2019; Gubin et al., 2014; Ribas and Wolchok, 2018; Sharma et al., 2021; Wei et al., 2017, 2019). When used in combination, anti-PD-1 plus anti-CTLA-4 regimen results in numerically higher response rates and longer overall survivals than anti-PD1 monotherapy in advanced melanoma (Amaria et al., 2018; Larkin et al., 2019; Menzies et al., 2021). The PD-1 plus CTLA-4 combination has also shown promising efficacy in other tumor types (Sharma et al., 2021). However, since the combined ICB regimen is far more toxic than anti-PD1 monotherapy (Larkin et al., 2019), more knowledge about the differential effects and mechanisms of action of combined ICB versus anti-PD1 monotherapy is of paramount importance.

Trafficking of lymphocytes to tumors is critical for cancer immunity and immunotherapy with ICB, vaccines, or adoptive T cell therapy (Chen and Mellman, 2013; Ribas and Wolchok, 2018; Sharma et al., 2021). The presence of high numbers of CD8$^+$ T cells in the tumor microenvironment is associated with clinical response to ICB in metastatic melanoma (Tumeh et al., 2014). Activation and differentiation of tumor-specific CD8$^+$ T cells within the melanoma tumor microenvironment lead to their accumulation as terminally exhausted T cells in an antigen-driven process (Oliveira et al., 2021). Recent studies have linked the response to ICB to PD-1$^+$TCF-1$^+$ stem-like rather than terminally exhausted CD8$^+$ T cells (Miller et al., 2019; Sade-Feldman et al., 2018; Siddiqui et al., 2019). Other studies indicate

Please cite this article in press as: Asrir et al., Tumor-associated high endothelial venules mediate lymphocyte entry into tumors and predict response to PD-1 plus CTLA-4 combination immunotherapy, Cancer Cell (2022), https://doi.org/10.1016/j.ccell.2022.01.002

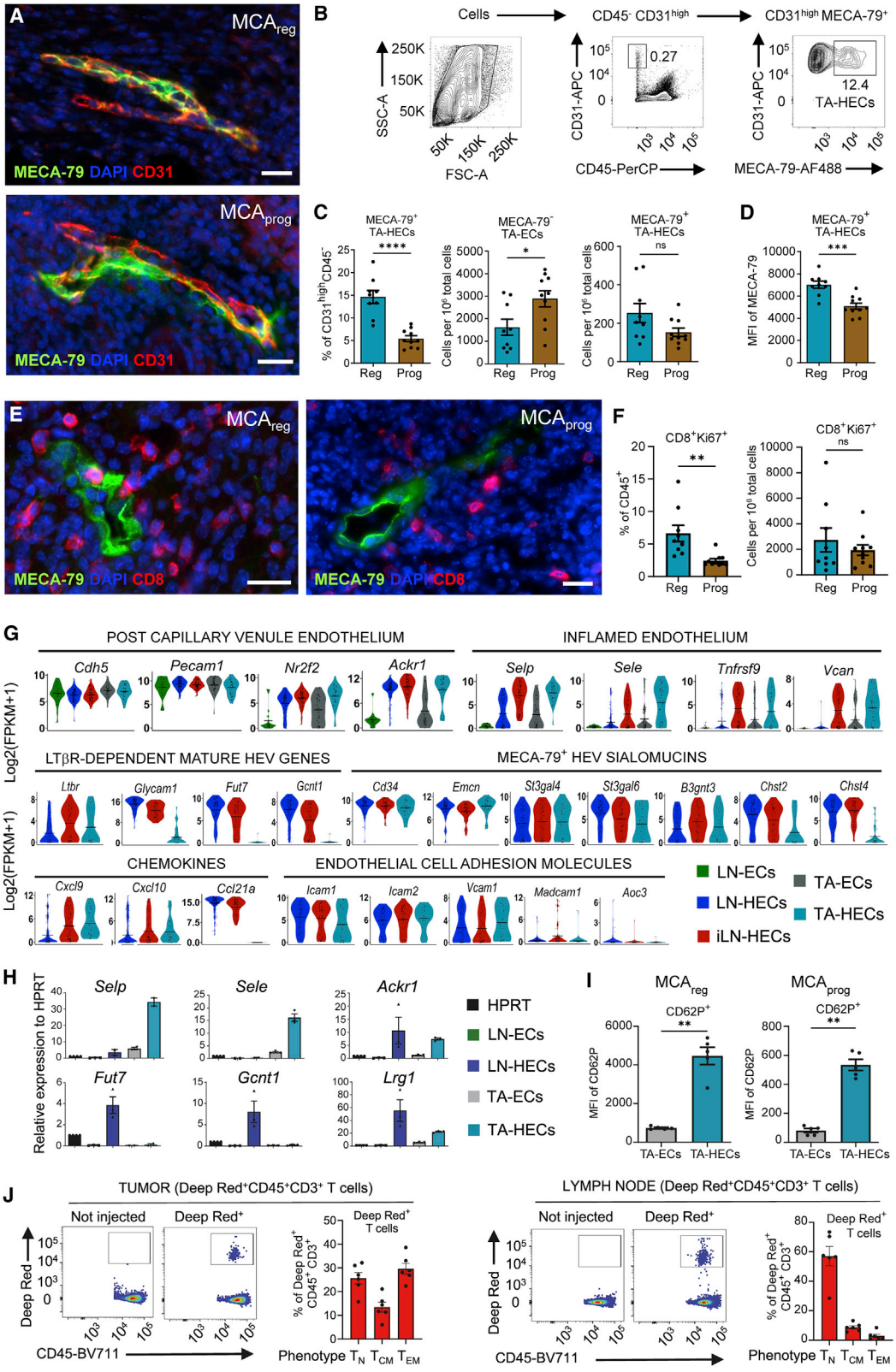

Figure 1. TA-HECs have a unique bifunctional hybrid phenotype and are associated with homing of naive, central memory, and effector T cells

(A) Immunofluorescence of MCA$_{reg}$ and MCA$_{prog}$ tumors (day 8) for MECA-79 (green) and CD31 (red), with DAPI (blue). Scale bar: 20 μm.

(B) Gating strategy for identification of TA-HECs by flow cytometry.

(legend continued on next page)

Please cite this article in press as: Asrir et al., Tumor-associated high endothelial venules mediate lymphocyte entry into tumors and predict response to PD-1 plus CTLA-4 combination immunotherapy, Cancer Cell (2022), https://doi.org/10.1016/j.ccell.2022.01.002

that activation of $CD8^+$ T cells in the peripheral compartment and their continuous recruitment into tumors may be important for clinical response (Brown and Wolchok, 2020; Dammeijer et al., 2020; Wu et al., 2020; Yost et al., 2019). Understanding the mechanisms governing lymphocyte recruitment into tumors at baseline and during ICB therapy is therefore crucial. Tumor blood vessels are known to limit extravasation of lymphocytes through multiple mechanisms (Buckanovich et al., 2008; Motz et al., 2014). In contrast, the mechanisms facilitating lymphocyte entry into tumors are less known. Although an important role of chemokines C-X-C motif chemokine ligand 9 (CXCL9) and CXCL10 has been demonstrated (Dangaj et al., 2019; Harlin et al., 2009; Mikucki et al., 2015; Peng et al., 2015; Spranger et al., 2017), the molecular and functional characteristics of tumor blood vessels mediating lymphocyte extravasation into tumors remain poorly defined.

High endothelial venules (HEVs) are specialized blood vessels for lymphocyte recruitment in lymph nodes and other lymphoid organs (Girard et al., 2012; Moussion and Girard, 2011). HEVs express high levels of sulfated sialomucins recognized by the lymphocyte homing receptor L-selectin (CD62L) and the HEV-specific antibody MECA-79 (Girard et al., 2012). MECA-79^+ HEV-like blood vessels (tumor-associated HEVs, TA-HEVs) are frequently observed in human solid tumors (Blanchard and Girard, 2021; Martinet et al., 2011, 2012). Their density correlates with densities of $CD3^+$ and $CD8^+$ T cells and $CD20^+$ B cells, as well as with favorable clinical parameters in primary breast cancer and melanoma (Martinet et al., 2011, 2012). TA-HEVs are present in tertiary lymphoid structures (TLSs) (Blanchard and Girard, 2021; Helmink et al., 2020; Petitprez et al., 2020) but are most often found in areas containing high densities of T cells and mature dendritic cells and in the absence of B cell-rich TLSs (Martinet et al., 2012, 2013). Induction of MECA-79^+ TA-HEVs has also been observed in several mouse tumor models, where it correlates with T cell infiltration and inhibition of tumor growth (Allen et al., 2017; Colbeck et al., 2017; Hindley et al., 2012; Johansson-Percival et al., 2017; Peske et al., 2015). Despite these important advances, MECA-79^+ TA-HEV endothelial cells (TA-HECs) remain poorly defined at the molecular and functional levels. Here, we sought to further characterize TA-HEVs and TA-HECs in order to provide a better understanding of the molecular mechanisms controlling lymphocyte entry into tumors during cancer immunity and immunotherapy.

RESULTS

TA-HECs are present at lower frequency in immunoedited tumors that escape the immune system

We first determined the impact of cancer immunoediting on TA-HEVs using methylcholanthrene (MCA)-induced mouse models of cancer (Figures S1A and S1B) (Gubin et al., 2014). Unedited immunogenic MCA_{reg} tumors derived from *Rag2*$^{-/-}$ mice spontaneously regress when transplanted into naive C57BL/6 wild-type mice (Figure S1A). MCA_{prog} tumors derived from wild-type mice have attenuated immunogenicity, due to immunoediting, and form progressively growing sarcomas when transplanted into naive wild-type recipients (Figure S1B). We observed MECA-79^+CD31^+ TA-HEVs in the microenvironment of both unedited MCA_{reg} and immunoedited MCA_{prog} tumors (Figure 1A). Endothelial cells lining these vessels (TA-HECs) exhibit a ''flat'' morphology different from the ''plump'' morphology generally observed in lymph node HEVs (Girard et al., 2012). We identified TA-HECs in tumor cell suspensions as $CD45^-CD31^{high}$MECA-79^+ cells and non-HEC tumor-associated ECs (TA-ECs) as $CD45^-CD31^{high}$MECA-79^- cells (Figure 1B). TA-HECs represented ~14 and 5% of $CD45^-CD31^{high}$ endothelial cells (ECs) in MCA_{reg} and MCA_{prog} tumors, respectively (Figure 1C). Numbers of TA-ECs were significantly lower in MCA_{reg} tumors. The mean fluorescence intensity (MFI) of MECA-79 staining is a good readout of the quality of HECs and their degree of maturity/functionality (Moussion and Girard, 2011). We found that TA-HECs in MCA_{reg} tumors had higher MECA-79 MFI than their counterparts in MCA_{prog} tumors (Figure 1D). In both tumor models, $CD8^+$ T cells were often present in clusters surrounding MECA-79^+ TA-HEVs in the periphery of the tumors (Figures 1E and S1C). The frequencies of $CD8^+Ki67^+$ T cells were higher in MCA_{reg} tumors (Figure 1F), but their numbers were only slightly increased (ns), probably because MCA_{reg} tumors were in a late stage of tumor regression at day 8 and

(C and D) Frequency and numbers of TA-HECs and TA-ECs (C), and MFI of MECA-79 (D) in MCA_{reg} and MCA_{prog} tumors (day 8), quantified by flow cytometry. Each symbol represents an individual mouse. Presented data were obtained from two independent experiments for a total of MCA_{reg} = 9 mice and MCA_{prog} = 10 mice. Data indicate means ± SEM.

(E) Immunofluorescence of MCA_{reg} (day 8) and MCA_{prog} (day 9) tumors for MECA-79 (green) and CD8 (red), with DAPI (blue). Scale bar: 20 μm.

(F) Percentage and number of $CD8^+Ki67^+$ T cells. Each symbol represents an individual mouse. Presented data were obtained from two independent experiments for a total of MCA_{reg} = 9 mice and MCA_{prog} = 10 mice. Data indicate means ± SEM.

(G) Violin plots showing the expression distribution of representative genes in the different endothelial cell subsets. Gene expression values were calculated as fragments per kilobase of transcript per million (FPKM).

(H) RT-qPCR analysis of selected genes in endothelial cell subsets isolated from MCA_{reg} tumors (day 7) or lymph nodes of WT mice. Data are shown as means ± SD. Each symbol represents an individual sample (n = 2 or 3).

(I) MFI of CD62P in TA-ECs and TA-HECs of MCA_{reg} and MCA_{prog} tumors (day 7), quantified by flow cytometry. Each symbol represents an individual mouse (TA-ECs = 5 mice, TA-HECs = 5 mice). Data indicate means ± SEM.

(J) Homing of fluorescent lymphocytes isolated from tumor-bearing mice (Deep Red^+) to MCA_{prog} tumors (day 7) or lymph nodes analyzed by flow cytometry after 1 h. The frequency of homed T cells with naive (T_N), central memory (T_{CM}), or effector/effector memory (T_{EM}) phenotypes was quantified. Presented data were obtained from two independent experiments for a total of n = 6 mice. Data indicate means ± SEM;

p values were determined by unpaired two-tailed Student's t test (C, D, and F) or two-tailed Mann-Whitney test (I). *$p < 0.05$; **$p < 0.01$; ***$p < 0.001$; ****$p < 0.0001$.

See also Figures S1–S3 and Tables S1 and S2.

contained large central areas devoid of $CD8^+$ T cells and $CD31^+$ ECs (Figure S1D). We concluded that, although their density is lower in immunoedited tumors, TA-HECs are associated with $CD8^+$ T cell infiltration in both unedited and immunoedited tumors.

TA-HECs derive from post-capillary venules and have a unique bifunctional hybrid phenotype

We used RNA-sequencing to compare TA-HECs with their counterparts in homeostatic (LN-HECs) or inflamed (iLN-HECs) lymph nodes (Veerman et al., 2019) and to MECA-79^- ECs (TA-ECs, LN-ECs) (Figure 1G). TA-HECs expressed post-capillary venule marker *Ackr1* (DARC) (Figure 1G) (Thiriot et al., 2017), and many genes characteristic of $DARC^+$ ECs (Figure S2A; Table S1) (von Andrian et al., 2015), indicating that they derive from post-capillary venule endothelium. Downregulated genes in TA-HECs include those encoding markers of arterial and capillary endothelium (Figure S2B) and endothelin B receptor (*Ednrb*; Figure S2C) that mediates the endothelial barrier to T cell homing to tumors (Buckanovich et al., 2008). Similar to iLN-HECs, TA-HECs expressed high levels of inflammatory genes (Figure 1G) and downregulated activity-dependent genes (Figure S2D). Among the 360 genes differentially expressed between iLN-HECs and LN-HECs, 250 were common between iLN-HECs and TA-HECs (Table S2). The molecular phenotype of TA-HECs was, however, unique, since TA-HECs expressed several genes not found or poorly expressed in other settings (Figure S2E).

A further comparison of the three HEC populations revealed that, although TA-HECs express *Ltbr*, lymphotoxin β receptor (LTβR)-dependent genes characteristic of the mature HEV phenotype (Veerman et al., 2019) were poorly expressed (Figure 1G), indicating a very immature HEV phenotype. Several genes implicated in the synthesis of MECA-79^+ HEV sialomucins (Girard et al., 2012) were equally expressed in all HEC populations, whereas genes encoding HEC sulfotransferases (*Chst2*, *Chst4*), were expressed at lower levels in TA-HECs (Figure 1G). TA-HECs expressed mRNAs encoding inflammatory chemokines CXCL9 and CXCL10, but did not express the mRNA encoding C-C motif chemokine ligand 21 (CCL21), a chemokine critical for recruitment of $CCR7^+$ naive and central memory lymphocytes (Girard et al., 2012). However, $CCL21^{high}$ cells surrounded TA-HEVs, and the chemokine was produced in tumors by $gp38^+CD31^-$ cells and $gp38^+CD31^+$ lymphatic ECs (Figure S2F and S2G). In human lymph nodes, CCL21 produced by perivascular cells rather than HECs is believed to translocate to the HEV lumen by transcytosis (Carlsen et al., 2005). A similar scenario may apply in tumors. Finally, the mRNAs encoding EC adhesion molecules intercellular adhesion molecule *1* (ICAM1), ICAM2, and vascular cell adhesion molecule 1 (VCAM1) important for lymphocyte sticking to HEVs (Girard et al., 2012) were expressed at similar levels in all HECs (Figure 1G).

We confirmed the unique phenotype of TA-HECs by using independently sorted EC samples (Figure 1H). *Selp* and *Sele,* encoding endothelial selectins CD62P and CD62E, were upregulated, whereas *Fut7* and *Gcnt1* were downregulated in TA-HECs compared with LN-HECs, and *Ackr1* was expressed similarly in both populations. All these genes were poorly expressed in LN-ECs and TA-ECs. Indeed, TA-HECs expressed more than 5-fold higher levels of *Selp* and *Sele* mRNAs than TA-ECs. Immunofluorescence staining revealed expression of CD62E (E-selectin) in TA-HEVs in MCA_{reg} tumors and inflamed lymph nodes but not in homeostatic lymph nodes (Figure S2H). Flow cytometry analysis (Figure S2I) showed significantly higher levels of CD62P (increased MFI) at the surface of TA-HECs compared with TA-ECs in both MCA_{reg} and MCA_{prog} tumors (Figure 1I). Together, these RNA and protein results indicated that TA-HEVs are the major sites of *Selp* and *Sele* expression in the tumor vasculature.

We next performed short-term homing assays and found that intravenously injected lymphocytes isolated from tumor-bearing mice (Figures 1J and S3A) or naive mice (Figure S3B) migrated to both tumors and lymph nodes. Phenotypic analyses of lymphocytes that homed to tumors revealed that TA-HEVs were associated with recruitment of both $CD62L^+$ and $CD62L^-$ T cell subsets, including cells with naive (T_N, $CD3^+CD62L^+CD44^-$), central memory (T_{CM}, $CD3^+CD62L^+CD44^+$), and effector/effector memory (T_{EM}, $CD3^+CD62L^-CD44^+$) phenotypes. In contrast, HEVs in lymph nodes were associated with homing of $CD62L^+$ T_N and T_{CM} subsets but not $CD62L^-$ T_{EM} subset.

Thus, TA-HECs expressed high levels of CD62E/CD62P and were associated with homing of $CD62L^-$ effector T cells. However, TA-HECs were distinct from ECs lining "classical" inflamed post-capillary venules because they co-expressed MECA-79^+-sulfated HEV sialomucins critical for recruitment of $CD62L^+$-naive and central memory T cells. TA-HECs were also clearly distinct from lymph node HECs, including iLN-HECs, because they had a very immature HEV phenotype due to limited expression of mature HEV genes. Therefore, we concluded that TA-HECs have a unique bifunctional hybrid phenotype.

CTLA-4 blockade increases the frequency of TA-HECs and the abundance of tumor-infiltrating $CD4^+$ and $CD8^+$ T cells

MCA_{prog} tumors grew faster in $Rag2^{-/-}$ mice, which lack adaptive immune cells, and frequency of TA-HECs was reduced (Figures S4A and S4B). Adoptive transfer of wild-type $CD3^+$ or $CD4^+$ T cells resulted in an increased frequency of TA-HECs (Figure S4C). Moreover, *in vivo* depletion experiments using anti-CD4 or anti-CD8 antibodies in wild-type mice revealed a critical role of endogenous $CD4^+$ T cells in TA-HEC induction in MCA_{prog} tumors (Figure 2A). Given the critical role of T cells in TA-HEC development, we next analyzed the impact of ICB therapy on TA-HECs in MCA_{prog} tumors (Figure 2B). We found that treatment with anti-CTLA-4, but not anti-PD-1, monotherapy increased the frequency of TA-HECs by reducing the numbers of TA-ECs, while maintaining a constant number of TA-HECs (Figure 2C). In addition, CTLA-4 monotherapy significantly increased the numbers of $CD4^+$ and $CD8^+$ T cells, and proliferating ($Ki67^+$) $CD4^+$ and $CD8^+$ T cells, and the frequency of $CD4^+$ and $CD8^+$ T cells producing IFNγ upon *ex vivo* activation (Figures 2D, 2E, S4D, and S4E). IFNγ production by activated tumor-specific T cells leads to the reactive expression of PD-L1 in the tumor microenvironment (Ribas and Wolchok, 2018; Spranger et al., 2013). We observed an increased frequency of $PD\text{-}L1^+$ cells and an increased expression of PD-L1 (MFI) in $PD\text{-}L1^+$ cells after CTLA-4 monotherapy, suggesting an increased abundance of activated tumor-specific T cells after

Please cite this article in press as: Asrir et al., Tumor-associated high endothelial venules mediate lymphocyte entry into tumors and predict response to PD-1 plus CTLA-4 combination immunotherapy, Cancer Cell (2022), https://doi.org/10.1016/j.ccell.2022.01.002

CellPress
OPEN ACCESS

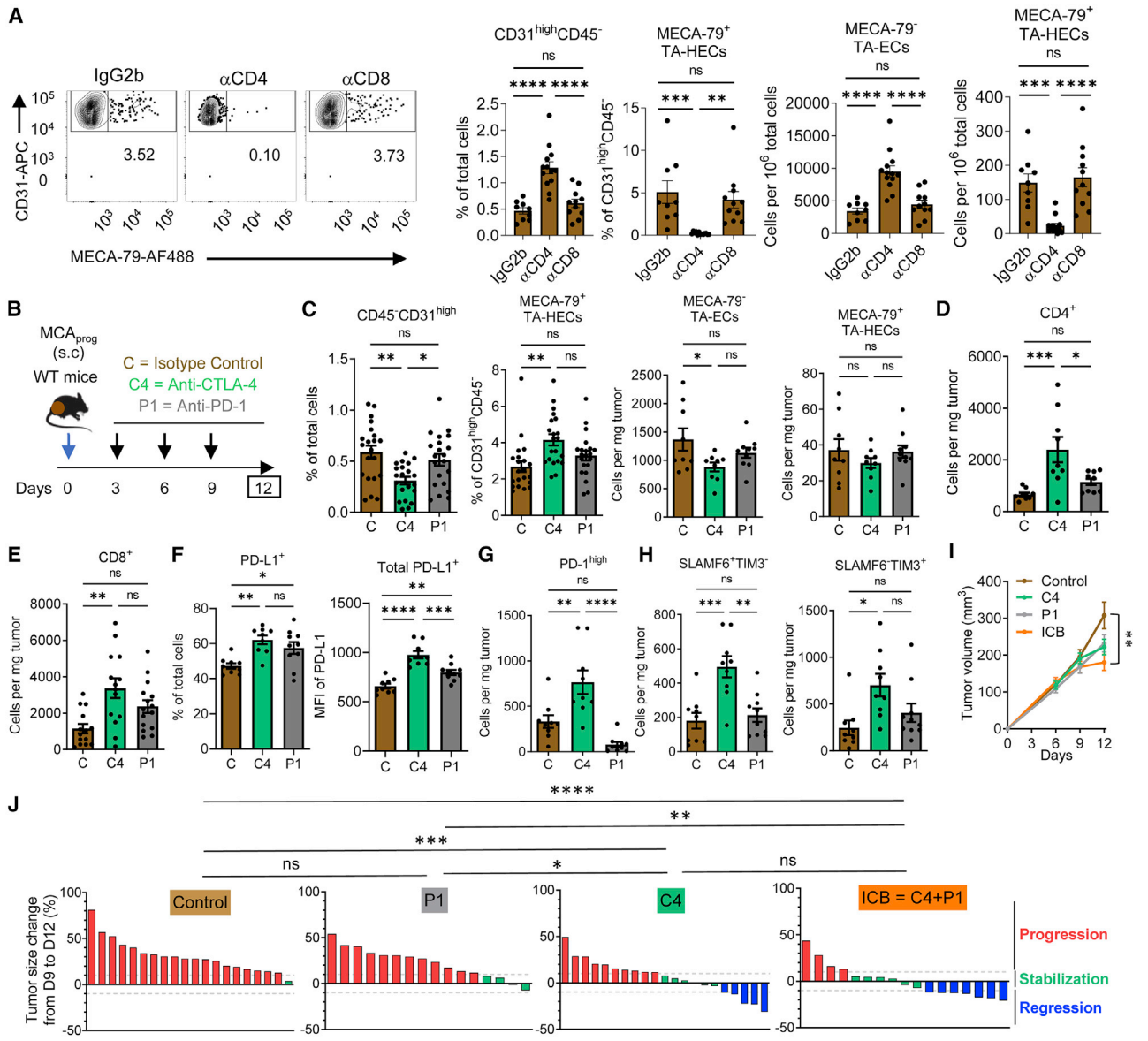

Figure 2. CTLA-4 blockade increases the frequency of TA-HECs and the abundance of tumor-infiltrating CD4 and CD8 T cells

(A) MCA_{prog} tumor-bearing mice (day 8) treated with isotype control (IgG2b), αCD4-, or αCD8-depleting antibodies. Frequencies and numbers of TA-ECs and TA-HECs are shown. Each symbol represents an individual mouse. Presented data were obtained from two independent experiments for a total of IgG2b = 9 mice, αCD4 = 13 mice, and αCD8 = 11 mice. Data indicate means ± SEM.

(B) Treatment schedule; s.c., subcutaneous.

(C) Frequencies and numbers of TA-ECs and TA-HECs. Each symbol represents an individual mouse. Presented data were obtained from six independent experiments at the left (total: C = 21 mice, C4 = 21 mice, P1 = 21 mice) and two experiments at the right (total: C = 9 mice, C4 = 9 mice, P1 = 10 mice). Data indicate means ± SEM.

(D and E) Numbers of $CD4^+$ (D) and $CD8^+$ T cells (E). Each symbol represents an individual mouse. Presented data in D were obtained from two independent experiments (total: C = 9 mice, C4 = 9 mice, P1 = 10 mice) and those in E from three experiments (total: C = 14 mice, C4 = 14 mice, P1 = 15 mice). Data indicate means ± SEM.

(F–H) Percentage and MFI of $PD\text{-}L1^+$ cells (F), and numbers of $CD8^+CD44^+PD\text{-}1^{high}$ T cells (G), and $SLAMF6^+TIM3^-$ and $SLAMF6^-TIM3^+$ T cells (H). Each symbol represents an individual mouse. Data in all panels are from two independent experiments (total: C = 9 mice, C4 = 9 mice, P1 = 10 mice). Data indicate means ± SEM.

(I and J) Mean tumor volumes (I), and tumor size changes in individual mice (J). Combined treatment group (ICB = anti-CTLA-4+ anti-PD-1) is included. Data are from five independent experiments in I (total: C = 19 mice, C4 = 22 mice, P1 = 18 mice, ICB = 22 mice) and from six experiments in J (total: C = 20 mice, P1 = 16 mice, C4 = 21 mice, ICB = 17 mice). Data indicate means ± SEM;

p values were determined by one-way ANOVA with Tukey's multiple comparison test (A and C–J). *p< 0.05; **p < 0.01; ***p < 0.001; ****p < 0.0001.

See also Figure S4.

Please cite this article in press as: Asrir et al., Tumor-associated high endothelial venules mediate lymphocyte entry into tumors and predict response to PD-1 plus CTLA-4 combination immunotherapy, Cancer Cell (2022), https://doi.org/10.1016/j.ccell.2022.01.002

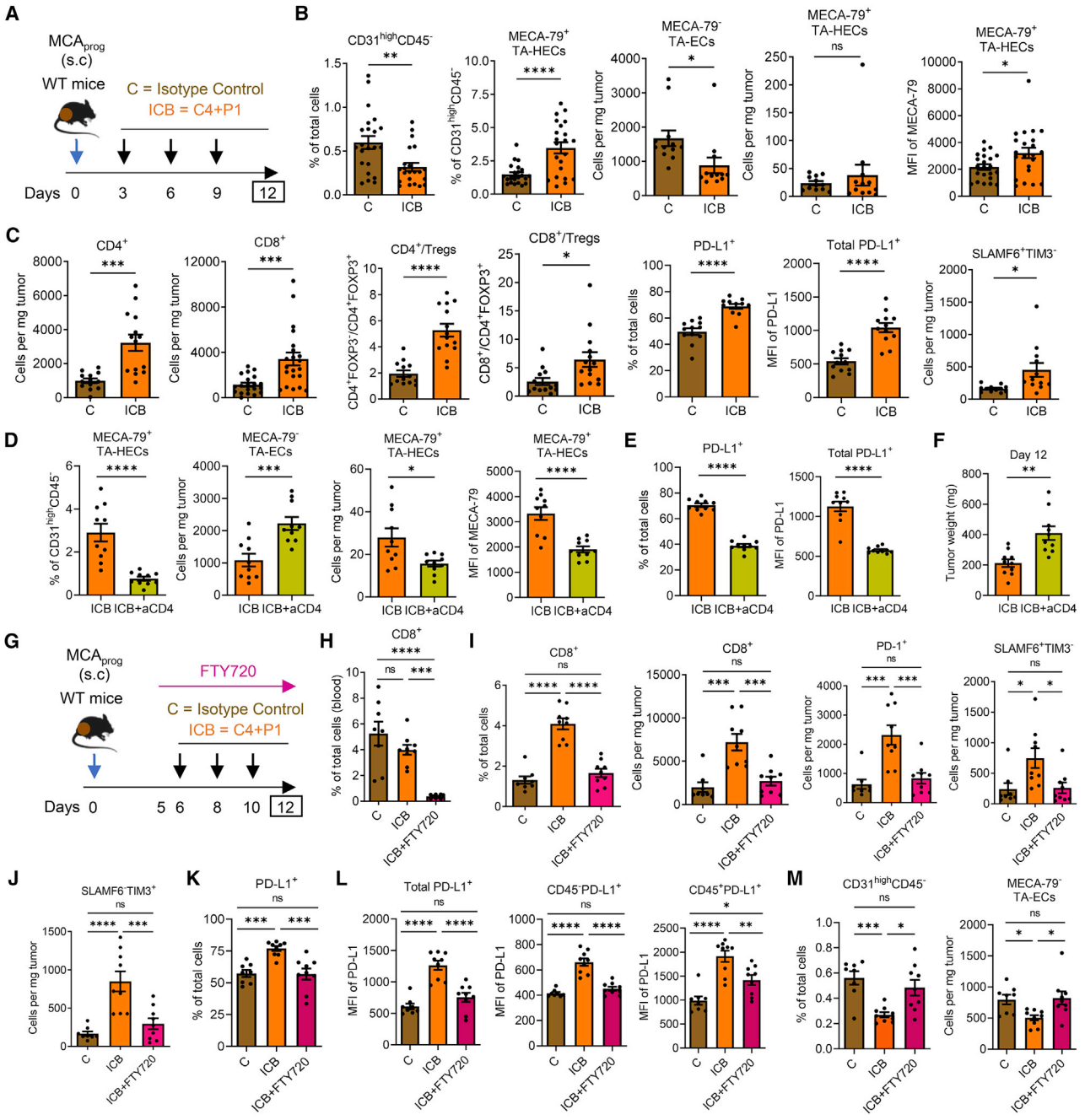

Figure 3. Combined ICB therapy increases TA-HEC frequency and promotes infiltration of CD8 T cells from the periphery

(A) Treatment schedule; s.c., subcutaneous; C4, anti-CTLA-4; P1, anti-PD-1.

(B) Frequencies and numbers of TA-ECs and TA-HECs, and MFI of MECA-79. Each symbol represents an individual mouse. Presented data were obtained from six independent experiments at the left and right (Total: C = 22 mice, ICB = 22 mice) and three experiments in the middle (total: C = 12 mice, ICB = 12 mice). Data indicate means ± SEM.

(C) Numbers of $CD4^+$ and $CD8^+$ T cells, $CD4^+/T_{regs}$ and $CD8^+/T_{regs}$ ratios, percentage and MFI of $PD\text{-}L1^+$ cells, and number of $SLAMF6^+TIM3^-$ T cells. Each symbol represents an individual mouse. Presented data were obtained from five independent experiments in the left $CD8^+$ (total: C = 20 mice, ICB = 21 mice) and three experiments in the left $CD4^+$ and middle (Total: C = 13 mice, ICB = 14 mice), and right (total: C = 12 mice, ICB = 12 mice). Data indicate means ± SEM.

(D–F) MCA_{prog} tumor-bearing mice (day 12) treated with ICB or ICB plus αCD4 depleting antibody (ICB+aCD4). (D) Frequencies and numbers of TA-ECs and TA-HECs, and MFI of MECA-79. (E) Percentage and MFI of $PD\text{-}L1^+$ cells. (F) Tumor weight. Each symbol represents an individual mouse. Data in all panels are from two independent experiments for a total of ICB = 10 mice and ICB+aCD4 = 10 mice. Data indicate means ± SEM.

(G–M) MCA_{prog} tumor-bearing mice (day 12) treated with isotype control (C), ICB or ICB plus FTY720 (ICB+FTY720). (G) Schema of treatment. (H) Percentage of $CD8^+$ T cells in blood. (I–K and M) Percentages and numbers of various cell subsets in tumors. (L) MFI of PD-L1. Each symbol represents an individual

(legend continued on next page)

treatment (Figure 2F). PD-1 monotherapy also had some impact on PD-L1 expression but CTLA-4 monotherapy had the strongest effect. Anti-CTLA-4 increased the numbers of PD-1^{+} and PD-1^{high} CD8^{+}CD44^{+} T cells, whereas anti-PD-1 increased the ratio of PD-1^{int} to PD-1^{high}CD8^{+}CD44^{+} T cells (Figures 2G and S4F–S4H). We then analyzed the influence of the treatments on stem-like (SLAMF6^{+}TIM3^{-}) and terminally exhausted (SLAMF6^{-}TIM3^{+}) CD8^{+} T cells (Figures S4G and S4I) (Miller et al., 2019). We found that CTLA-4 monotherapy, but not PD-1 monotherapy, increased the numbers of both stem-like and terminally exhausted CD8^{+} T cells (Figure 2H). The expansion of terminally exhausted T cells suggested an increased anti-tumor response after anti-CTLA-4 treatment.

Finally, we analyzed the impact of CTLA-4 and PD-1 monotherapies and PD-1 plus CTLA-4 combined ICB on tumor growth. All treatments inhibited tumor growth, but the combined therapy had a stronger inhibitory effect and resulted in a higher number of mice responding to therapy (tumor stabilization or regression) compared with the monotherapies (Figures 2I and 2J). We thus selected the combined ICB therapy for the following part of our studies.

Combined ICB therapy increases TA-HEC frequency and promotes infiltration of CD8^{+} T cells from the periphery

We found that combined ICB treatment (Figure 3A) increased the frequency of TA-HECs and MECA-79 MFI and reduced the numbers of TA-ECs (Figure 3B). Increased frequency of TA-HECs after combined ICB was associated with elevated frequency and numbers of tumor-infiltrating CD4^{+} and CD8^{+} T cells and proliferating CD4^{+} and CD8^{+} T cells, higher ratios of CD4^{+}FOXP3^{-} T cells to CD4^{+}FOXP3^{+}-regulatory T cells (Tregs) and CD8^{+} T cells to Tregs, increased frequency and MFI of PD-L1^{+} cells, and increased numbers of stem-like and terminally exhausted CD8^{+} T cells (Figures 3C and S5A–S5C). Furthermore, treatment with dual ICB increased the numbers of PD-1^{+} and PD-1^{int} CD8^{+}CD44^{+} T cells and the ratio of PD-1^{int} to PD-1^{high} CD8^{+}CD44^{+} T cells (Figure S5D). The numbers of intratumoral CD8^{+} T cells and stem-like CD8^{+} T cells correlated with the frequencies of MECA-79^{+} TA-HECs and were higher in tumors containing high frequencies of TA-HECs (Figures S5E and S5F).

Next, we investigated the role of CD4^{+} T cells in TA-HEC regulation in ICB-treated tumors. Depletion of CD4^{+} T cells during ICB resulted in increased numbers of TA-ECs and reduced numbers and MECA-79 MFI of TA-HECs (Figures 3D and S5G). Numbers of CD4^{+} T cells in tumors were strongly reduced (as expected), and there was also a trend (ns) for reduced numbers of CD8^{+} T cells (Figure S5H). The frequency and MFI of PD-L1^{+} total cells, CD45^{-} (tumor and stromal) cells, and CD45^{+} (immune) cells decreased significantly (Figures 3E and S5I), and tumor weight increased (Figure 3F). Thus, CD4^{+} T cells regulate TA-HEC numbers and reactive expression of PD-L1, and limit tumor growth during ICB therapy of MCA$_{prog}$ tumors.

The increased TA-HEC frequency after ICB suggested that T cell trafficking from the periphery might contribute to the increased numbers of CD8^{+} T cells in ICB-treated tumors. We thus performed additional experiments with the S1P receptor inhibitor FTY720, which inhibits lymphocyte recirculation (Spitzer et al., 2017). Treatment was initiated 1 day prior to ICB to inhibit migration caused by ICB (Figure 3G). FTY720 treatment decreased circulating CD8^{+} T cells in peripheral blood (Figure 3H) and prevented the increase in the numbers of tumor-infiltrating CD8^{+} T cells, PD-1^{+}CD8^{+} T cells, and stem-like and terminally exhausted CD8^{+} T cells, induced by combined ICB therapy (Figures 3I and 3J). Importantly, FTY720 treatment also prevented the ICB-induced increase in PD-L1^{+} cells frequency and PD-L1 MFI in PD-L1^{+} total cells, CD45^{-} cells, and CD45^{+} cells (Figures 3K and 3L), and the ICB-induced decrease in the frequency of ECs and the numbers of TA-ECs (Figure 3M). We concluded that T cell trafficking from the periphery is required for ICB-induced changes (increased numbers of CD8^{+} T cells, reactive expression of PD-L1, modulation of tumor blood vessels) in the tumor microenvironment.

TA-HEVs are the main sites of lymphocyte tethering, rolling, and sticking in the tumor microcirculation

We next used *in vivo* imaging to analyze the capacity of TA-HEVs to mediate lymphocyte extravasation into MCA$_{prog}$ tumors treated with combined ICB therapy. TA-HEVs were visualized in living mice by use of intravascular staining with non-blocking amounts of fluorescently labeled MECA-79 mAb (Moussion and Girard, 2011). Positive staining with MECA-79 mAb after i.v. injection indicated that MECA-79^{+} HEV sialomucins are expressed at the luminal surface of the vessels (Figure 4A). The mean diameter of TA-HEVs (~40 μm) was similar to that of order III HEVs in lymph nodes (von Andrian, 1996) and was not modified by ICB (Figure 4B). We used intravital epifluorescence microscopy in real-time to visualize the interactions of calcein-labeled lymphocytes with TA-HEVs inside the tumor microcirculation (Figures 4C and S6A). We analyzed the first critical steps in the lymphocyte/HEV endothelium adhesion cascade (Girard et al., 2012), lymphocyte rolling after initial tethering to the vessel wall, and firm arrest (sticking) on the endothelium (Video S1; Figure 4D). The percentage of lymphocytes that rolled along the walls of intratumoral blood vessels (rolling fraction) in tumor-bearing mice treated with combined ICB was close to 40% in MECA-79^{+} TA-HEVs but was <10% in MECA-79^{-} non-HEV blood vessels (Figure 4E). The rolling velocity of these cells was heterogeneous, and their median rolling speed (Figure S6B) was higher than that of naive lymphocytes in order III HEVs in lymph nodes (Moussion and Girard, 2011). Treatment with αCD62L/L-selectin and αPSGL-1 antibodies, which blocked lymphocyte receptors for MECA-79^{+} HEV sialomucins and endothelial E/P-selectins, respectively, revealed an important role of these two adhesion pathways in the initial tethering and rolling interactions of lymphocytes with TA-HEVs. We then measured the fraction of

mouse. Data in all panels are from two independent experiments for a total of C = 8 mice, ICB = 9 mice and ICB+FTY720 = 9 mice. Data indicate means ± SEM;

p values were determined by unpaired two-tailed Student's t test (B–F) or one-way ANOVA with Tukey's multiple comparison test (H–M). *p < 0.05; **p < 0.01; ***p < 0.001; ****p < 0.0001.

See also Figure S5.

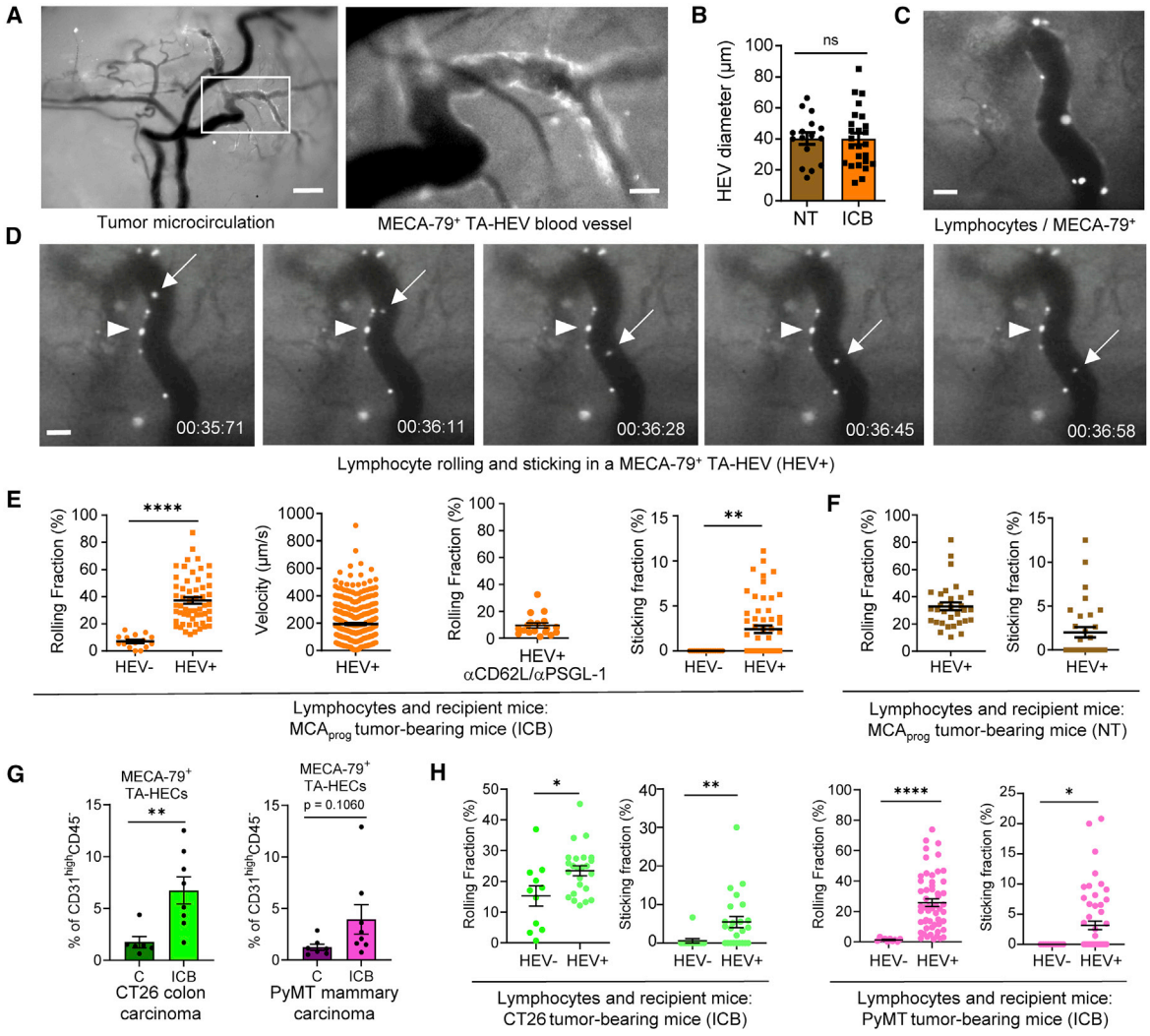

Figure 4. TA-HEVs are the main sites of lymphocyte tethering, rolling, and sticking in the tumor microcirculation

(A–F) Intravital microscopy analyses of TA-HEVs in MCA_{prog} tumors from mice not treated (NT, day 8) or treated with ICB (anti-CTLA-4 + anti-PD-1) (day 12). (A) TA-HEVs are revealed by intravascular staining with fluorescent MECA-79 mAb. Scale bars: 200 µm (left), 50 µm (right). (B) TA-HEV diameter. Each symbol represents an individual blood vessel. Data are from two (NT = 16 HEV+ vessels) or three (ICB = 25 HEV+ vessels) experiments. Data indicate means ± SEM. (C and D) Interactions of calcein-labeled lymphocytes with a TA-HEV visualized in real time. Scale bars: 50 µm. Arrows denote a rolling cell and arrowheads a sticking cell (D). (E and F) Rolling fraction, rolling velocity, and sticking fraction in TA-HEVs (HEV+) or MECA-79⁻ blood vessels (HEV–). In some experiments, transferred lymphocytes were pre-treated with αCD62L and αPSGL-1 function-blocking antibodies (E). Each symbol represents an individual blood vessel, except for the velocity panel, where symbols represent individual cells. Presented data in E were obtained from three independent experiments (rolling and sticking fractions, total: HEV+ = 56 vessels, 5 mice and HEV- = 15 vessels, 5 mice; velocity, total: HEV+ = 326 lymphocytes, 56 vessels, 5 mice) or four experiments (rolling fraction with αCD62L and αPSGL-1, total: HEV+ = 18 vessels, 4 mice). Presented data in F were obtained from three independent experiments (total: HEV+ = 31 vessels, 4 mice). Data indicate means ± SEM.

(G and H) CT26 and PyMT tumors (day 12) treated with isotype control (C) or ICB, as shown in Figure 3A. (G) Frequencies of TA-HECs. Each symbol represents an individual mouse. Presented data were obtained from four independent experiments for the CT26 panel (Total: C = 6 mice, ICB = 8 mice) and three experiments for the PyMT panel (total: C = 7 mice, ICB = 8 mice). Data indicate means ± SEM.

(H) Rolling and sticking fractions. Each symbol represents an individual blood vessel. Presented data were obtained from two independent experiments (CT26, total: HEV+ = 24 vessels, 3 mice and HEV– = 11 vessels, 3 mice; PyMT, total: HEV+ = 54 vessels, 3 mice and HEV– = 10 vessels, 3 mice). Data indicate means ± SEM;

p values were determined by two-tailed Mann-Whitney test (E and H) or unpaired two-tailed Student's t test (B and G). *p < 0.05; **p < 0.01; ****p < 0.0001. See also Figure S6 and Video S1.

lymphocytes that transitioned from rolling to firm arrest (sticking fraction). This sticking fraction was close to zero in MECA-79⁻ non-HEV tumor blood vessels; most, if not all, sticking events occurred in MECA-79⁺ TA-HEVs. These observations indicated that TA-HEVs constitute the major sites of lymphocyte arrest in the microvasculature of MCA_{prog} tumors treated with combined ICB. We measured similar rolling and sticking fractions of lymphocytes isolated from untreated tumor-bearing or

naive mice in MECA-79$^+$ TA-HEVs in tumor-bearing mice not treated or treated with ICB (Figures 4F and S6C–S6E). Thus, TA-HEVs mediate lymphocyte recruitment at baseline, in the absence of ICB treatment. Finally, we performed intravital microscopy analyses with CD62L$^-$ lymphocytes isolated from MCA_{prog} tumor-bearing mice treated with dual ICB and enriched for CD8$^+$ T cells. We observed that these CD62L$^-$ lymphocytes tethered, rolled, stuck, and stably arrested in MECA-79$^+$ TA-HEVs in ICB-treated MCA_{prog} tumors (Figures S6F and S6G). Together, these *in vivo* imaging experiments indicated that TA-HEVs were major sites of lymphocyte capture and arrest in the MCA_{prog} tumor microcirculation, both at baseline and during combined ICB therapy.

We then extended our observations to two other tumor models and genetic backgrounds: CT26 colon carcinomas in BALB/c mice, and PyMT mammary carcinomas in FvB mice. We detected higher levels of CD62P expression on TA-HECs compared with TA-ECs in both tumor models (Figure S6H), indicating that this is a conserved feature of the TA-HEC phenotype across different models. We found that combined ICB increases the frequency and numbers of TA-HECs in both models, although this did not achieve statistical significance in the PyMT model (Figures 4G and S6I). Intravital microscopy revealed that MECA-79$^+$ TA-HEVs were the major sites of lymphocyte rolling and sticking in the microcirculation of ICB-treated CT26 tumors, although lymphocyte rolling also occurred in MECA-79$^-$ blood vessels (Figure 4H). Strikingly, lymphocyte rolling and sticking occurred exclusively in TA-HEVs in PyMT mammary carcinomas treated with combined ICB. We concluded that TA-HEVs are the main sites of lymphocyte arrest in the tumor microvasculature during combined ICB therapy in various mouse tumor models and genetic backgrounds.

TA-HEVs mediate lymphocyte entry into tumors treated with combined ICB therapy

We next set up multiphoton *in vivo* imaging approaches to study the later steps of the recruitment cascade (Girard et al., 2012) in MECA-79$^+$ TA-HEVs. Analysis of TA-HEVs from MCA_{prog} tumor-bearing mice treated with dual ICB revealed that, after arrest, lymphocytes crawled on the endothelium surface (Video S2; Figure 5A) before entering the tumor tissue by crossing TA-HEV walls (Video S3; Figure 5B). Similarly, lymphocytes crawled and extravasated through TA-HEVs in the microcirculation of ICB-treated CT26 colon carcinomas (Video S4; Figure 5B) and PyMT mammary carcinomas (Video S5; Figure 5B). Together, the results of the intravital and multiphoton imaging experiments demonstrated that TA-HEVs functioned as major portals for lymphocytes to enter tumors.

Although ICB treatment did not appear to markedly modify the capacity of TA-HEVs to capture lymphocytes (Figures 4E and 4F), the results were not directly comparable because the intravital microscopy experiments were performed at different time points (baseline, day 8; ICB, day 12). To complement the *in vivo* imaging studies, we thus performed additional functional experiments. We first analyzed lymphocyte homing and observed that short-term lymphocyte homing was significantly increased in ICB-treated MCA_{prog} tumors (both homing ratio and ratio of fluorescent lymphocytes per TA-HEC; Figure 5C). We next performed experiments with blocking antibodies against CD62L and PSGL-1 (Block), and found that this treatment prevented the increase in CD8$^+$ and CD4$^+$ T cells in the tumor after ICB (Figures 5D–5F). Together, these data provided functional evidence that ICB changes the efficacy of TA-HEVs, and that TA-HEV-mediated entry of peripheral lymphocytes into tumor plays a major role in the increased abundance of tumor-infiltrating T cells after ICB.

Increasing TA-HEC frequency and maturation reduces CD8$^+$ T cell exhaustion and increases the proportion of stem-like CD8$^+$ T cells

Our *in vivo* imaging experiments demonstrated convincingly that TA-HEVs were functional in tumors. However, our transcriptomic analyses indicated that TA-HECs exhibited a very immature HEV phenotype. To induce more mature TA-HECs, we thus treated MCA_{prog} tumors with a LTβR agonistic antibody (Allen et al., 2017). When used as a monotherapy (i.t.) (Figure 6A), the LTβR agonistic antibody did not change the numbers of TA-ECs, but increased the frequency and numbers of TA-HECs, and their maturation, as revealed by the enhanced MECA-79 MFI (Figure 6B). Treatment had similar effects in *Rag2*$^{-/-}$ mice, supporting a direct effect of the antibody on ECs expressing LTβR, independently of adaptive immune cells (Figures S7A and S7B). Increased frequency and maturation of TA-HECs after treatment of wild-type mice was associated with reduced tumor weight (Figure 6C) but not with a significant change in the percentage and numbers of CD8$^+$ T cells (Figure 6D). CD8$^+$ T cells and B220$^+$ B cells were associated with MECA-79$^+$ TA-HEVs in the periphery of tumors treated with the LTβR agonistic antibody, but formation of B cell-rich TLSs was not observed (Figure 6E). We next determined the impact of the treatment on CD8$^+$ T cell subsets (Figure 6F). Monotherapy with the LTβR agonistic antibody significantly reduced the frequency and numbers of PD-1^{high}CD8$^+$ exhausted T cells and terminally exhausted CD8$^+$ T cells, and increased the proportion of stem-like CD8$^+$ T cells and the ratio of stem-like to terminally exhausted CD8$^+$ T cells (SLAMF6$^+$/TIM3$^+$), which had been associated with ICB response in melanoma patients (Sade-Feldman et al., 2018). We concluded that increasing HEV differentiation in tumors reduced CD8$^+$ T cell exhaustion and resulted in an increased proportion of stem-like CD8$^+$ T cells.

Increasing TA-HEC frequency and maturation ameliorates the efficacy of combined ICB therapy

We next treated MCA_{prog} tumor-bearing mice with dual ICB (i.p.) in combination with the LTβR agonistic antibody (i.t.) (Figure 7A). This triple treatment reduced the numbers of TA-ECs and increased the frequency, numbers, and MECA-79 MFI of TA-HECs (Figure 7B). Increased frequency and numbers of TA-HECs after triple therapy were associated with elevated frequency and numbers of tumor-infiltrating CD8$^+$ T cells and PD-1^{int}CD8$^+$ T cells, higher ratio of PD-1^{int} to PD-1^{high}CD8$^+$ T cells, and increased numbers of stem-like CD8$^+$ T cells (Figures 7C and S7C). The numbers of terminally exhausted CD8$^+$ T cells were not significantly modified by the treatment. The triple therapy also induced the reactive expression of PD-L1 in the tumor microenvironment (Figures 7D and S7D).

In another series of experiments, we co-administered (i.p.) dual ICB with the LTβR agonistic antibody (Figure 7E). We found that

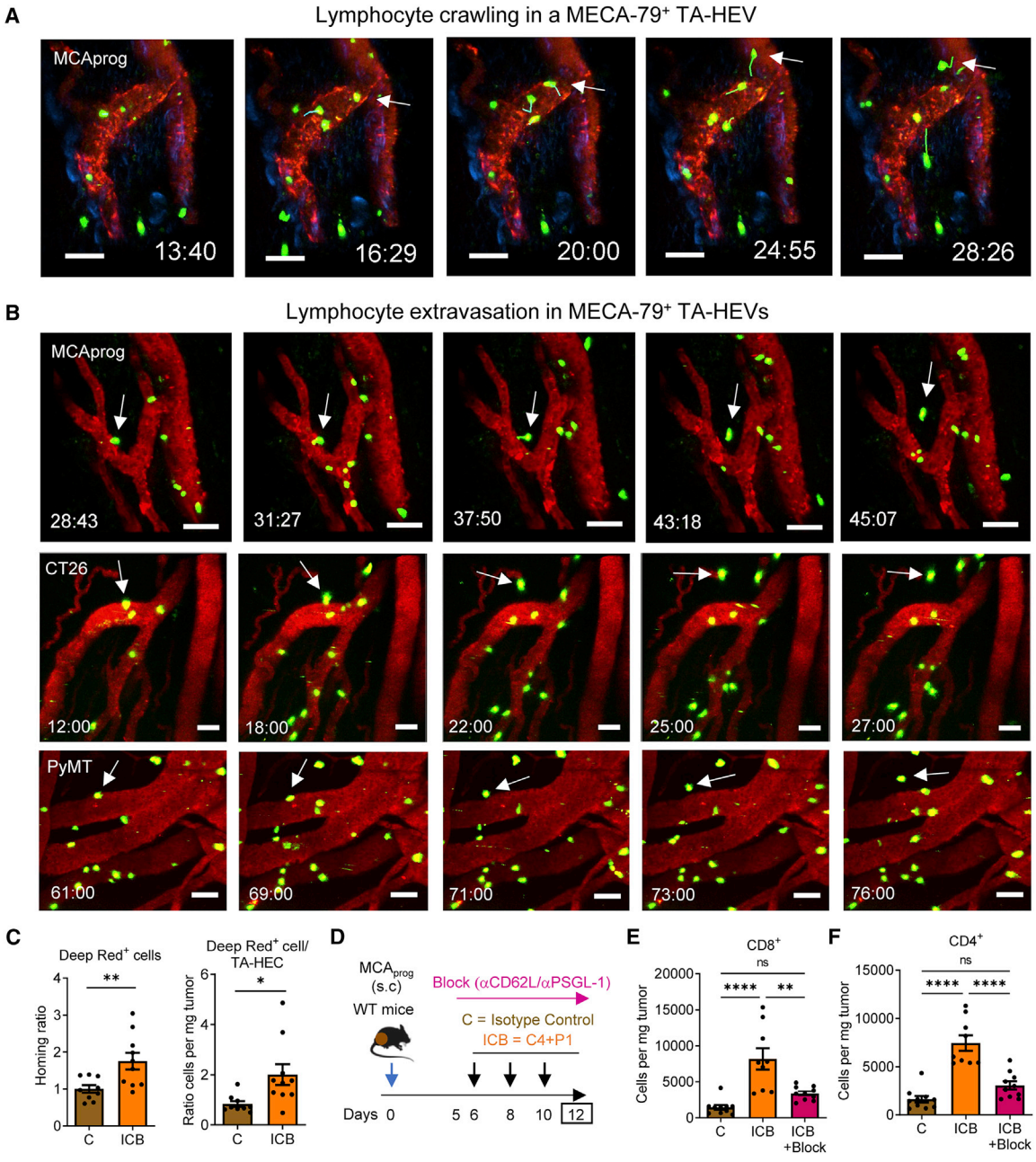

Figure 5. TA-HEVs mediate lymphocyte entry into tumors treated with combined ICB therapy

Figure360▷ For a Figure360 author presentation of this figure, see https://doi.org/10.1016/j.ccell.2022.01.002.

(A and B) Two-photon microscopy time-lapse images showing lymphocyte crawling (A) and extravasation (B) through MECA-79$^+$ TA-HEVs in MCA$_{prog}$, CT26 and PyMT tumors treated with ICB (anti-CTLA-4 + anti-PD-1, day 12). (A) Trajectories of calcein-labeled lymphocytes (green) crawling on TA-HEV endothelium are indicated. (B) Arrows denote lymphocytes (green) that cross TA-HEV walls. Blood vessels are labeled in red with Qtracker-565 (A and B) and collagen structures are labeled in blue (A). Wide-field intravital microscopy with non-blocking amounts of fluorescent MECA-79 mAb was used to identify TA-HEVs in the tumor microcirculation. Time in min/s. Scale bars: 50 μm.

(C) Homing of fluorescent lymphocytes isolated from tumor-bearing mice (Deep Red$^+$ cells) to MCA$_{prog}$ tumors (day 12), analyzed by flow cytometry after 1 h. Each symbol represents an individual mouse. Presented data were obtained from two independent experiments for a total of C = 9 mice and ICB = 10 mice. Data indicate means ± SEM.

(D–F) MCA$_{prog}$ tumor-bearing mice treated with ICB and Block (αCD62L/αPSGL-1 mAbs). (D) Schema of treatment. C4 = anti-CTLA-4; P1 = anti-PD-1. (E and F) Numbers of CD8$^+$ T cells (E) and CD4$^+$ T cells (F). Each symbol represents an individual mouse. Presented data were obtained from two independent experiments for a total of C = 10 mice, ICB = 9 mice and ICB + Block = 10 mice. Data indicate means ± SEM;

p values were determined by unpaired two-tailed Student's t test (C) or one-way ANOVA with Tukey's multiple comparison test (E and F). *$p < 0.05$; **$p < 0.01$; ****$p < 0.0001$.

See also Videos S2, S3, S4, and S5.

Please cite this article in press as: Asrir et al., Tumor-associated high endothelial venules mediate lymphocyte entry into tumors and predict response to PD-1 plus CTLA-4 combination immunotherapy, Cancer Cell (2022), https://doi.org/10.1016/j.ccell.2022.01.002

CellPress
OPEN ACCESS

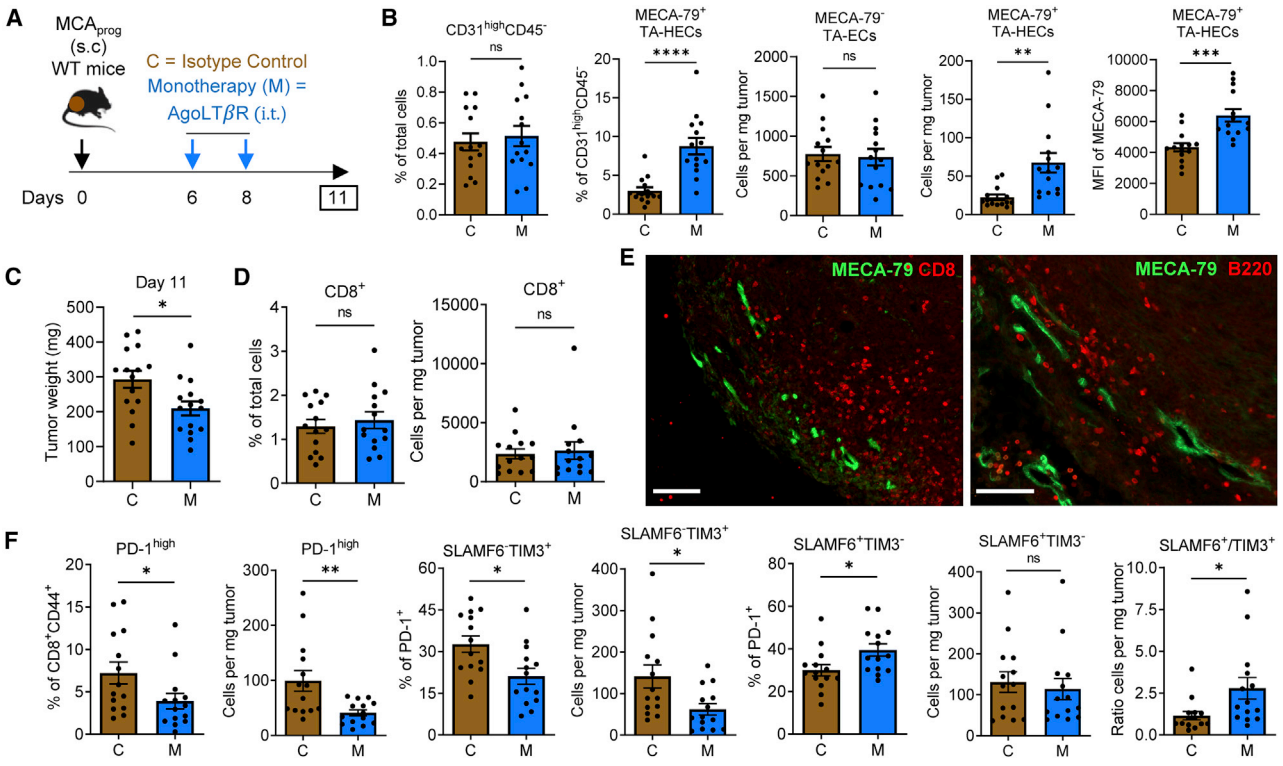

Figure 6. Increasing TA-HEC frequency and maturation reduces CD8$^+$ T cell exhaustion and increases the proportion of stem-like CD8$^+$ T cells

(A) Treatment schedule; i.t., intratumoural.

(B) Frequencies and numbers of TA-ECs and TA-HECs, and MFI of MECA-79. Each symbol represents an individual mouse. Data in all panels are from three independent experiments for a total of C = 14 mice and M = 14 mice. Data indicate means ± SEM.

(C and D) Tumor weight (C), and percentage and number of CD8$^+$ T cells (D). Each symbol represents an individual mouse. Data are from three independent experiments in C (total: C = 15 mice, M = 15 mice) and three experiments in D (total: C = 14 mice, M = 14 mice). Data indicate means ± SEM.

(E) Immunofluorescence of MCA$_{prog}$ tumors treated with M (day 11), for MECA-79 (green) and CD8 (red) or B220 (red). Scale bars: 100 μm.

(F) Percentages and numbers of PD-1^{high} cells among CD8$^+$CD44$^+$ T cells, SLAMF6$^-$TIM3$^+$ and SLAMF6$^+$TIM3$^-$ cells, and ratio of SLAMF6$^+$TIM3$^-$ to SLAMF6$^-$TIM3$^+$ T cells. Each symbol represents an individual mouse. Data in all panels are from three independent experiments for a total of C = 14 mice and M = 14 mice. Data indicate means ± SEM;

p values were determined by unpaired two-tailed Student's t test (B–D and F). *p< 0.05; **p< 0.01; ***p < 0.001; ****p < 0.0001.

See also Figure S7.

this triple combination reduced the numbers of TA-ECs and increased the frequency and numbers of TA-HECs (Figures 7F and S7E). It also increased the maturation of TA-HECs, as shown by the upregulated expression of LTβR-dependent mature HEV genes (*Glycam1*, *Fut7*) (Figure 7G). *B3gnt3*, which is critical for synthesizing MECA-79 antigens but is not known to be regulated by LTβR signaling (Veerman et al., 2019), was also induced after the treatment. MECA-79$^+$ TA-HEVs were frequent in the tumor microenvironment, particularly at the periphery of the tumors (Figure 7H), and were often lined by endothelial cells exhibiting a plump morphology (Figure 7I), reminiscent of HECs lining HEVs in lymph nodes (Girard et al., 2012). Importantly, the triple therapy induced regression of MCA$_{prog}$ tumors (Figure 7J) and increased the percentage of mice responding to treatment (Figure 7K; 9/13 mice with regressing tumors, 69%) compared with combined ICB (Figure 2J; 7/17 mice with regressing tumors, 41%). We concluded that triple therapy with combined ICB and the LTβR agonistic antibody induced a more mature HEV phenotype in TA-HECs in association with increased ICB efficacy.

TA-HEVs are predictive for better response and survival of metastatic melanoma patients treated with combined ICB therapy

Building on the above results from mouse tumor models, we examined whether TA-HEVs might be predictive for response to ICB in patients. We analyzed the presence of MECA-79$^+$ TA-HEVs in pre-treatment lesions from a large cohort of patients (n = 93) with unresectable stage III or IV metastatic melanoma treated with an anti-PD-1 antibody (nivolumab or pembrolizumab) as a single-agent (n = 65) or in combination with an anti-CTLA-4 antibody (ipilimumab; n = 28) (Table S3). We observed TA-HEVs in skin/subcutaneous (Figure 8A) and lymph node tumor biopsies in association with CD8$^+$ T cell infiltration (Figure S8A). TA-HEV scores were significantly higher in clinical responders (R) than in non-responders (NR) in the overall cohort (p = 0.0105) and in the subgroup of patients treated with combined ICB (p = 0.0101) but not in the subgroup of patients treated with PD-1 monotherapy (p = 0.3454) (Figure 8B). There was a trend for higher CD8$^+$ T cell densities in clinical responders in all subgroups of patients, but it did

Please cite this article in press as: Asrir et al., Tumor-associated high endothelial venules mediate lymphocyte entry into tumors and predict response to PD-1 plus CTLA-4 combination immunotherapy, Cancer Cell (2022), https://doi.org/10.1016/j.ccell.2022.01.002

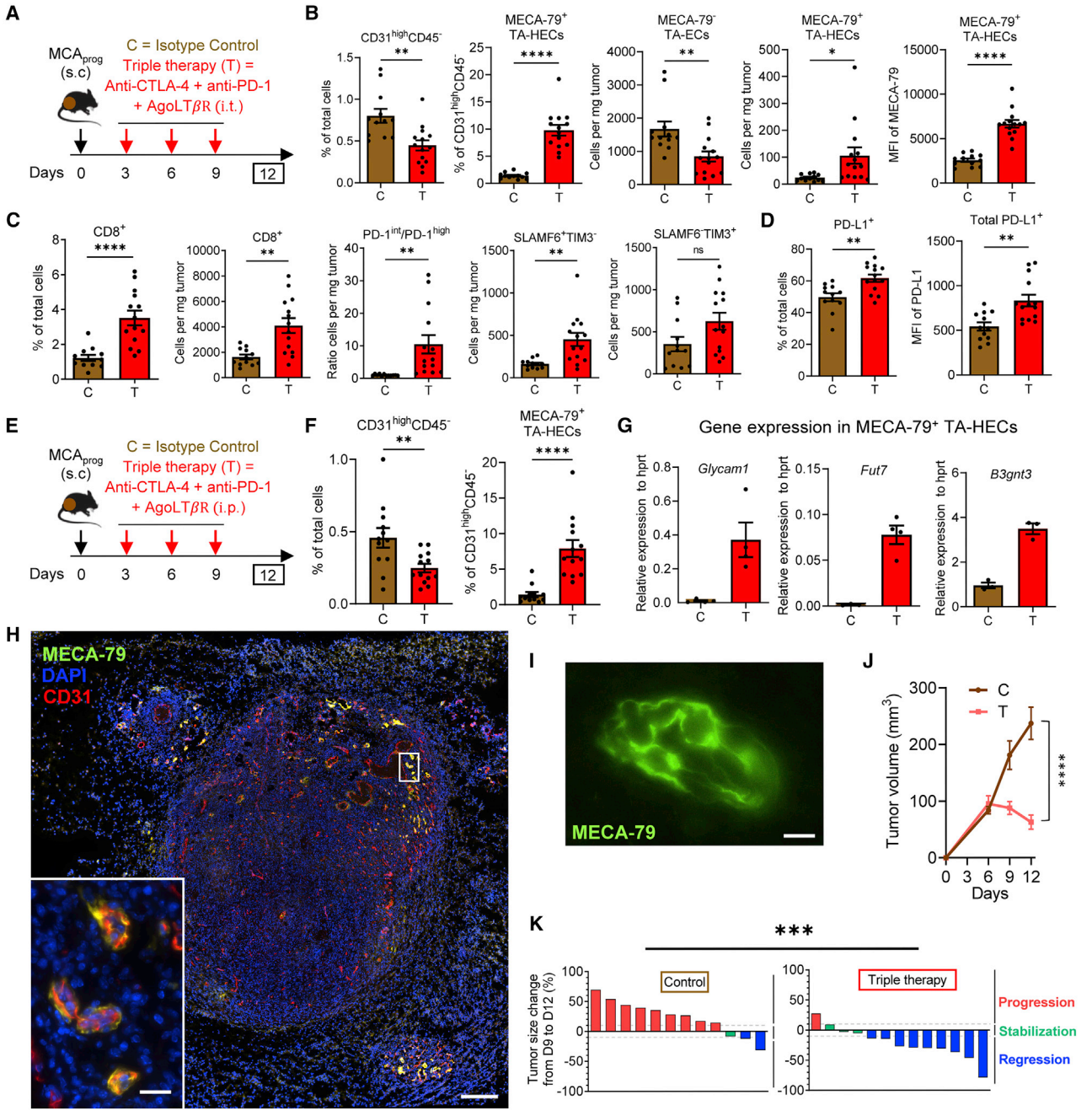

Figure 7. Increasing TA-HEC frequency and maturation ameliorates the efficacy of combined ICB therapy

(A–D) Treatment with isotype control (C) or triple therapy combining anti-CTLA-4 + anti-PD-1 and i.t. LTβR agonistic mAb (T). (A) Treatment schedule with i.t. LTβR agonistic mAb starting at day 6. (B) Frequencies and numbers of TA-ECs and TA-HECs, and MFI of MECA-79. (C and D) Percentage, number, ratio or MFI of various cell subsets in tumors. Each symbol represents an individual mouse. Data in all panels are from three independent experiments for a total of C = 12 mice and T = 14 mice. Data indicate means ± SEM.

(E–K) Treatment with isotype control (C) or triple therapy combining anti-CTLA-4, anti-PD-1 and i.p. LTβR agonistic mAb (T). (E) Treatment schedule with i.p. LTβR agonistic mAb starting at day 3. (F) Frequencies of $CD45^{-}CD31^{high}$ cells and TA-HECs. Each symbol represents an individual mouse. Data are from four independent experiments for a total of C = 12 mice and T = 13 mice. Data indicate means ± SEM. (G) RT-qPCR analysis of the expression of selected genes in TA-HECs isolated from MCA_{prog} tumors. Data are shown as means ± SD. Each symbol represents an individual sample (n = 3 or 4). (H and I) Immunofluorescence of MCA_{prog} tumor treated with T (day 9) for MECA-79 (green) and CD31 (red), with DAPI (blue). The inset shows a higher-magnification image of the boxed area. Scale bars: 200 μm (H), 20 μm (H, inset), 5 μm (I). (J and K) Mean tumor volume (J), and changes in tumor size in individual mice (K). Data are from four independent experiments for a total of C = 12 mice and T = 13 mice. Data in J indicate means ± SEM;

(legend continued on next page)

Please cite this article in press as: Asrir et al., Tumor-associated high endothelial venules mediate lymphocyte entry into tumors and predict response to PD-1 plus CTLA-4 combination immunotherapy, Cancer Cell (2022), https://doi.org/10.1016/j.ccell.2022.01.002

CellPress
OPEN ACCESS

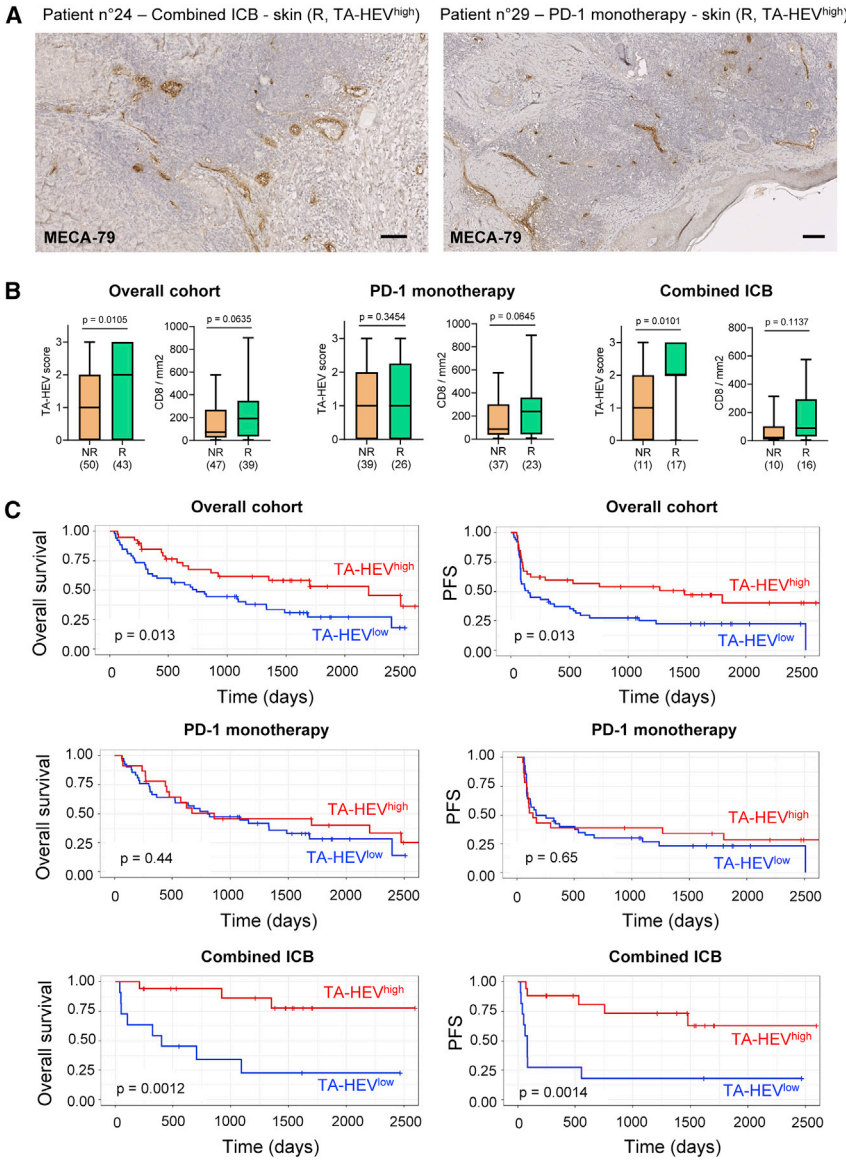

Figure 8. TA-HEVs are predictive for better response and survival of metastatic melanoma patients treated with combined ICB therapy

(A) Immunostaining of MECA-79$^+$ TA-HEVs in skin lesions from metastatic melanoma patients collected before treatment. Scale bars: 100 μm.

(B) Quantification of TA-HEVs and CD8$^+$ T cells in responders (R) and non-responders (NR) to treatment. Numbers of R and NR patients are indicated. Bars indicate median values, and error bars denote IQR; p values were determined by unpaired two-tailed Student's t test.

(C) Kaplan-Meier analyses of overall survival and progression-free survival (PFS) according to TA-HEV scores. Overall cohort: TA-HEV^{high} (n = 40), TA-HEV^{low} (n = 53); PD-1 monotherapy: TA-HEV^{high} (n = 23), TA-HEV^{low} (n = 42); combined ICB: TA-HEV^{high} (n = 17), TA-HEV^{low} (n = 11); p values were calculated by log rank test.

See also Figure S8 and Table S3.

not reach statistical significance (Figure 8B). To further dissect the impact of TA-HEVs on patient response, we stratified the cohort into patients with high and low TA-HEV scores in tumor lesions. A high TA-HEV score was significantly associated with response in the overall cohort (p = 0.021) and in the subgroup treated with combined ICB (p = 0.004), but not in the subgroup treated with PD-1 single-agent (p = 0.672) (Figure S8B). Moreover, Kaplan-Meier survival analyses in the overall cohort (Figure 8C) revealed that patients having lesions with high TA-HEV scores had better overall survival (OS, p = 0.013) and progression-free survival (PFS, p = 0.013) than those whose tumors had low TA-HEV scores. This association of high TA-HEV scores with improved OS and PFS was largely driven by the subgroup treated with combined ICB (OS, p = 0.0012; PFS, p = 0.0014), with a non-significant association in the subgroup treated with PD-1 monotherapy (OS, p = 0.44; PFS, p = 0.65). In contrast to the TA-HEV scores, high densities of CD8$^+$ T cells did not predict OS and PFS in the overall cohort and the subgroup treated with combined ICB (Figure S8C). We concluded that high numbers of TA-HEVs in melanoma lesions are associated with better clinical response and survival of patients treated with combined ICB therapy.

DISCUSSION

In this study, we show that MECA-79$^+$ TA-HEVs function as major sites of lymphocyte extravasation into tumors during cancer immunity and immunotherapy with immune checkpoint inhibitors. Intravital imaging in three different mouse tumor models and genetic backgrounds revealed that lymphocytes were arrested in the tumor microcirculation almost exclusively in TA-HEVs during combined anti-PD-1/anti-CTLA-4 immunotherapy and used a multistep adhesion cascade (tethering, rolling, sticking, crawling, *trans*-endothelial migration) to extravasate through TA-HEVs. We also observed lymphocyte rolling and sticking at baseline, indicating that TA-HEVs mediate lymphocyte recruitment both at baseline and during ICB treatment. The density of TA-HEVs, which depends on tumor immunogenicity, could thus be a good indicator of the

p values were determined by unpaired two-tailed Student's t test (B–D and F). *p < 0.05; **p < 0.01; ***p < 0.001; ****p < 0.0001. Some individual data points in controls (B–D) are identical to those of Figures 3B, 3C, S5C, and S5D, because several T and ICB experiments were performed simultaneously with a single control experiment.

See also Figure S7.

intrinsic ability of a tumor to attract new lymphocytes continuously. We demonstrate that TA-HECs derive from post-capillary venules, exhibit an immature HEV phenotype, co-express MECA-79$^+$ HEV sialomucins and high levels of E/P-selectins, and are associated with homing into tumors of both L-selectin$^+$ (naive, central memory) and L-selectin$^-$ (effector/effector memory) T cells, and increased infiltration of CD4$^+$ and CD8$^+$ T cells, including stem-like CD8$^+$ T cells. We found that treatment with an agonistic antibody against LTβR, a critical regulator of the mature HEV phenotype (Moussion and Girard, 2011), increased the frequency and maturation of TA-HECs, improved the efficacy of combined ICB therapy, and induced a higher proportion of stem-like CD8$^+$ T cells and a higher ratio of stem-like to terminally exhausted T cells, two characteristics previously associated with ICB efficacy and prolonged survival in human melanoma patients (Miller et al., 2019; Sade-Feldman et al., 2018). Thus, although our imaging studies revealed that TA-HECs are functional at baseline, these later results indicated that it is important to increase TA-HEC maturation in order to improve the efficacy of cancer immunotherapy. Together, our data suggest that TA-HEVs may be the main sites of entry into tumors for various subsets of lymphocytes (naive, central memory, effector/effector memory, stem-like) critical for anti-tumor immunity and response to ICB. These results also support the possibility that the presence of high numbers of TA-HEVs in primary tumors and metastases may favorably affect anti-tumor immunity and responses to immunotherapies by increasing the number of newly recruited lymphocytes that are primed and/or activated toward tumor antigens locally at the tumor site.

We uncovered an important role of CD4$^+$ T cells in the regulation of TA-HEC frequencies and numbers in the MCA_{prog} tumor model, both at baseline and during ICB therapy. Moreover, we found that numbers of TA-ECs decreased and frequency of TA-HECs increased after anti-CTLA-4 blockade and dual ICB, but not after anti-PD-1 monotherapy. Thus, anti-CTLA-4-containing regimens reduce TA-ECs with poor recruitment capacity and preserve TA-HECs with high recruitment capacity. The abundance of tumor-infiltrating CD4$^+$ and CD8$^+$ T cells increased after anti-CTLA-4 monotherapy (or dual ICB), as previously observed in patients with melanoma, prostate cancer, and bladder cancer (Gao et al., 2017; Sharma et al., 2019). These T cells proliferated in tumors, produced IFNγ upon activation, and induced the reactive expression of PD-L1 on both CD45$^-$ and CD45$^+$ cells within the tumor microenvironment. Importantly, the reactive expression of PD-L1 and the decrease of TA-ECs, observed after combined ICB treatment, were no longer observed in the presence of FTY720, indicating that these changes are caused by tumor-reactive T cells newly recruited from the periphery rather than by tumor-resident T cells. The increase in various subsets of CD8$^+$ T cells, including stem-like and terminally exhausted CD8$^+$ T cells, that are generated from tumor-reactive stem-like T cells within the tumor microenvironment (Eberhardt et al., 2021; Jansen et al., 2019; Oliveira et al., 2021), was also abrogated by FTY720. Together with our homing assays, experiments with blocking antibodies against CD62L and PSGL-1, and intravital microscopy analyses, these later results indicate that TA-HEV-mediated entry of peripheral lymphocytes into tumors occurs continuously during ICB and plays a major role in the increased abundance of tumor-infiltrating T cells. We thus believe that the presence of TA-HEVs at baseline is important for the increased infiltration of peripheral lymphocytes into tumors after anti-CTLA-4 or anti-CTLA-4 + anti-PD-1 combination. Moreover, the results also suggest that the increased frequency of TA-HECs after CTLA-4 blockade or combined ICB, and the increased efficacy of TA-HEV-mediated lymphocyte homing after ICB, may contribute to the broadening of the tumor-specific T cell repertoire through enhanced recruitment of diverse T cell specificities from the peripheral compartment.

Increased frequency of TA-HECs after various treatments correlated with increased numbers of intratumoral T cells and/or better tumor control, but not always with increased numbers of TA-HECs. Similar to TA-HEC frequency, the maturity of TA-HECs increased under various conditions and was associated with increased abundance of tumor-infiltrating T cells and/or reduced tumor growth. Thus, our data indicate that the frequency and maturity of TA-HECs, in addition to TA-HEC numbers, are important for TA-HEV-mediated lymphocyte recruitment. Moreover, other parameters could modify lymphocyte recruitment through TA-HEVs and/or the abundance of T cells following TA-HEV-mediated entry into tumors. These include the upregulation of chemokines CXCL9 and CXCL10 (Dangaj et al., 2019; Harlin et al., 2009; Spranger et al., 2017), the reactivity of T cells with tumor (*neo*)antigens, the expansion of the newly recruited T cells after ICB, and their death or survival in the tumor microenvironment (Chen and Mellman, 2013; Ribas and Wolchok, 2018).

We quantified MECA-79$^+$ TA-HEVs in pre-treatment metastatic melanoma lesions in a large cohort (n = 93) of patients undergoing ICB therapy and found that high numbers of TA-HEVs predicted both treatment response and patient survival in the overall cohort and in the subgroup of patients treated with combined ICB therapy. In contrast, a high TA-HEV score did not predict response and survival in the subgroup of patients treated with anti-PD-1 monotherapy. These observations are consistent with the distinct mechanisms of anti-PD-1 and anti-CTLA-4 antibodies (Ribas and Wolchok, 2018; Sharma et al., 2021; Wei et al., 2017). PD-1 blockade is believed to act primarily at the tumor site (Tumeh et al., 2014), whereas anti-CTLA-4 treatment is known to broaden the melanoma-reactive CD8$^+$ T cell repertoire in the periphery (Kvistborg et al., 2014). Anti-CTLA-4 or dual ICB may thus be more dependent on TA-HEV-mediated lymphocyte recruitment into tumors than PD-1 blockade, which is more dependent on a pre-existing intratumoral T cell repertoire. However, recent results indicate that activation of CD8$^+$ T cells in the peripheral compartment (generation of tumor-specific stem-like CD8$^+$ T cells), particularly in tumor-draining lymph nodes, and recruitment of novel tumor-specific T cell clonotypes in the tumor may also be important for response to PD-1 blockade, at least in some patients or tumor types (Dammeijer et al., 2020; Wu et al., 2020; Yost et al., 2019). These latter mechanisms, which are likely to be more efficient in the presence of anti-CTLA-4 antibodies, may provide a scientific rationale for the increased efficacy of anti-PD-1 plus anti-CTLA-4 combination immunotherapy that has been reported in various tumor types and that we observed in our mouse tumor model.

In conclusion, our results provide important insights into the molecular and functional features of TA-HECs and their role in lymphocyte entry into tumors during cancer immunity and immunotherapy. In addition, they show that TA-HEVs are associated with better response and survival of metastatic melanoma patients treated with combined ICB therapy. Increasing the density and maturation of MECA-79^{+} TA-HECs in the tumor microenvironment could enhance lymphocyte trafficking to tumors and improve the efficacy of cancer immunotherapies.

STAR★METHODS

Detailed methods are provided in the online version of this paper and include the following:

- KEY RESOURCES TABLE
- RESOURCE AVAILABILITY
  - Lead contact
  - Materials availability
  - Data and code availability
- EXPERIMENTAL MODEL AND SUBJECT DETAILS
  - Patients
  - Mice
  - Cell lines
- METHOD DETAILS
  - Tumor transplantation and tumor volume and weight measurements
  - *In vivo* treatments
  - T cell depletion
  - Adoptive T cell transfer
  - Preparation of single cell suspensions from tumors and lymph nodes
  - Flow cytometry and cell sorting
  - Immunofluorescence staining of mouse tissues
  - Immunohistochemistry of human melanoma samples
  - Real-time qPCR (RT-qPCR)
  - Short-term homing assays
  - Wide-field intravital microscopy
  - Multiphoton *in vivo* imaging
  - Transcriptome profiling by RNA sequencing
- QUANTIFICATION AND STATISTICAL ANALYSIS

SUPPLEMENTAL INFORMATION

Supplemental information can be found online at https://doi.org/10.1016/j.ccell.2022.01.002.

ACKNOWLEDGMENTS

We thank L. Martinet for advice and initial observations, M. Pichery and E. Mirey for preliminary results, and members of the Girard laboratory for helpful discussions. We are grateful to Genotoul core facilities, ANEXPLO-IPBS, Microscopy and Cytometry TRI-IPBS, Cytometry TRI-I2MC, Imaging TRI-INRA, GeT-Santé, GeT-PlaGe, and Bioinfo. We acknowledge the help of E Näser, A. Zakaroff-Girard, and E. Riant for cytometry and cell sorting, J.J. Maoret, C. Genthon, and O. Bouchez for RNA-seq, C. Pouzet for the scanning of slides, E. Lefrançais for i.v. injections, and F. Viala for preparation of final figures. We thank R. Schreiber and Z. Werb for providing tumor cell lines. This work was supported by grants from Fondation ARC pour la Recherche sur le Cancer (SL220110603471, PGA 120150202411, and PGA1 RF20180206911 to J.-P.G.), Institut National du Cancer (INCa_2013-098 and INCa_2017-155 to J.-P.G.), Agence Nationale de la Recherche (ANR-12-BSV1-0006-01 to J.-P.G.), IDEX UNITI (ATS 2014 to J.-P. G.) and Laboratoire d'Excellence Toulouse Cancer (LABEX TOUCAN). C.T., J.C., R.L., L.B., and E.V. were supported by fellowships from LABEX TOUCAN, Fondation ARC (DOC20170505820), French Ministry of Research, and Fondation pour la Recherche Médicale (FRM FDT20160435636, ECO201806006827, ECO202006011469, and FDT202106012889). The Imaging Core Facility TRI-IPBS received financial support from ITMO Cancer Aviesan within the framework of Cancer Plan. This manuscript was edited at Life Science Editors. The graphical abstract was created with BioRender.com.

AUTHOR CONTRIBUTIONS

J.-P.G. conceived the study, supervised the work, and analyzed all the data. A.A., C.T., J.C., R.L., and L.B. performed the majority of experiments and analyzed the data. E.B. performed all intravital and multiphoton microscopy experiments and analyzed the data. K.V. assisted with RNA-seq experiments. S.B., F.L., E.V., and D.T. assisted in experiments with MCA tumor models. F.M. prepared the cDNA libraries for RNA-seq. S.R., I.G., I.M., and J.-Y.S. performed the analyses of clinical specimens. N.O. performed immunostaining of human TA-HEVs and analyzed the data. C.R. conceived and analyzed association with clinical data. J.-P.G. wrote the manuscript with inputs from A.A., C.T., J.C., R.L., L.B., E.B., N.O., and C.R. All authors discussed the results and commented on the manuscript.

DECLARATION OF INTERESTS

C.R. is an occasional consultant to Bristol Myers Squibb, Roche, Amgen, Novartis, Pierre Fabre, MSD, Sanofi, Biothera, CureVac, and Merck. All other authors have no competing interests.

Received: April 9, 2021
Revised: July 23, 2021
Accepted: January 7, 2022
Published: February 3, 2022

REFERENCES

Allen, E., Jabouille, A., Rivera, L.B., Lodewijckx, I., Missiaen, R., Steri, V., Feyen, K., Tawney, J., Hanahan, D., Michael, I.P., et al. (2017). Combined antiangiogenic and anti-PD-L1 therapy stimulates tumor immunity through HEV formation. Sci. Transl Med. *9*, eaak9679.

Amaria, R.N., Reddy, S.M., Tawbi, H.A., Davies, M.A., Ross, M.I., Glitza, I.C., Cormier, J.N., Lewis, C., Hwu, W.J., Hanna, E., et al. (2018). Neoadjuvant immune checkpoint blockade in high-risk resectable melanoma. Nat. Med. *24*, 1649–1654.

Blanchard, L., and Girard, J.P. (2021). High endothelial venules (HEVs) in immunity, inflammation and cancer. Angiogenesis *24*, 719–753.

Bolger, A.M., Lohse, M., and Usadel, B. (2014). Trimmomatic: a flexible trimmer for Illumina sequence data. Bioinformatics *30*, 2114–2120.

Brown, C.C., and Wolchok, J.D. (2020). PD-L1 blockade therapy: location, location, location. Cancer Cell *38*, 615–617.

Buckanovich, R.J., Facciabene, A., Kim, S., Benencia, F., Sasaroli, D., Balint, K., Katsaros, D., O'Brien-Jenkins, A., Gimotty, P.A., and Coukos, G. (2008). Endothelin B receptor mediates the endothelial barrier to T cell homing to tumors and disables immune therapy. Nat. Med. *14*, 28–36.

Carlsen, H.S., Haraldsen, G., Brandtzaeg, P., and Baekkevold, E.S. (2005). Disparate lymphoid chemokine expression in mice and men: no evidence of CCL21 synthesis by human high endothelial venules. Blood *106*, 444–446.

Chen, D.S., and Mellman, I. (2013). Oncology meets immunology: the cancer-immunity cycle. Immunity *39*, 1–10.

Colbeck, E.J., Jones, E., Hindley, J.P., Smart, K., Schulz, R., Browne, M., Cutting, S., Williams, A., Parry, L., Godkin, A., et al. (2017). Treg depletion licenses T cell-driven HEV neogenesis and promotes tumor destruction. Cancer Immunol. Res. *5*, 1005–1015.

Dammeijer, F., van Gulijk, M., Mulder, E.E., Lukkes, M., Klaase, L., van den Bosch, T., van Nimwegen, M., Lau, S.P., Latupeirissa, K., Schetters, S.,

et al. (2020). The PD-1/PD-L1-checkpoint restrains T cell immunity in tumor-draining lymph nodes. Cancer Cell *38*, 685–700.e8.

Dangaj, D., Bruand, M., Grimm, A.J., Ronet, C., Barras, D., Duttagupta, P.A., Lanitis, E., Duraiswamy, J., Tanyi, J.L., Benencia, F., et al. (2019). Cooperation between constitutive and inducible chemokines enables T cell engraftment and immune attack in solid tumors. Cancer Cell *35*, 885–900.e810.

Diamond, M.S., Kinder, M., Matsushita, H., Mashayekhi, M., Dunn, G.P., Archambault, J.M., Lee, H., Arthur, C.D., White, J.M., Kalinke, U., et al. (2011). Type I interferon is selectively required by dendritic cells for immune rejection of tumors. J. Exp. Med. *208*, 1989–2003.

Eberhardt, C.S., Kissick, H.T., Patel, M.R., Cardenas, M.A., Prokhnevska, N., Obeng, R.C., Nasti, T.H., Griffith, C.C., Im, S.J., Wang, X., et al. (2021). Functional HPV-specific PD-1(+) stem-like CD8 T cells in head and neck cancer. Nature *597*, 279–284.

Eisenhauer, E.A., Therasse, P., Bogaerts, J., Schwartz, L.H., Sargent, D., Ford, R., Dancey, J., Arbuck, S., Gwyther, S., Mooney, M., et al. (2009). New response evaluation criteria in solid tumours: revised RECIST guideline (version 1.1). Eur. J. Cancer *45*, 228–247.

Gao, J., Ward, J.F., Pettaway, C.A., Shi, L.Z., Subudhi, S.K., Vence, L.M., Zhao, H., Chen, J., Chen, H., Efstathiou, E., et al. (2017). VISTA is an inhibitory immune checkpoint that is increased after ipilimumab therapy in patients with prostate cancer. Nat. Med. *23*, 551–555.

Gide, T.N., Quek, C., Menzies, A.M., Tasker, A.T., Shang, P., Holst, J., Madore, J., Lim, S.Y., Velickovic, R., Wongchenko, M., et al. (2019). Distinct immune cell populations define response to anti-PD-1 monotherapy and anti-PD-1/anti-CTLA-4 combined therapy. Cancer Cell *35*, 238–255.e236.

Girard, J.P., Moussion, C., and Forster, R. (2012). HEVs, lymphatics and homeostatic immune cell trafficking in lymph nodes. Nat. Rev. Immunol. *12*, 762–773.

Gubin, M.M., Zhang, X., Schuster, H., Caron, E., Ward, J.P., Noguchi, T., Ivanova, Y., Hundal, J., Arthur, C.D., Krebber, W.J., et al. (2014). Checkpoint blockade cancer immunotherapy targets tumour-specific mutant antigens. Nature *515*, 577–581.

Halpern, J., Lynch, C.C., Fleming, J., Hamming, D., Martin, M.D., Schwartz, H.S., Matrisian, L.M., and Holt, G.E. (2006). The application of a murine bone bioreactor as a model of tumor: bone interaction. Clin. Exp. Metastasis *23*, 345–356.

Harlin, H., Meng, Y., Peterson, A.C., Zha, Y., Tretiakova, M., Slingluff, C., McKee, M., and Gajewski, T.F. (2009). Chemokine expression in melanoma metastases associated with CD8+ T-cell recruitment. Cancer Res. *69*, 3077–3085.

Helmink, B.A., Reddy, S.M., Gao, J., Zhang, S., Basar, R., Thakur, R., Yizhak, K., Sade-Feldman, M., Blando, J., Han, G., et al. (2020). B cells and tertiary lymphoid structures promote immunotherapy response. Nature *577*, 549–555.

Hindley, J.P., Jones, E., Smart, K., Bridgeman, H., Lauder, S.N., Ondondo, B., Cutting, S., Ladell, K., Wynn, K.K., Withers, D., et al. (2012). T-cell trafficking facilitated by high endothelial venules is required for tumor control after regulatory T-cell depletion. Cancer Res. *72*, 5473–5482.

Jansen, C.S., Prokhnevska, N., Master, V.A., Sanda, M.G., Carlisle, J.W., Bilen, M.A., Cardenas, M., Wilkinson, S., Lake, R., Sowalsky, A.G., et al. (2019). An intra-tumoral niche maintains and differentiates stem-like CD8 T cells. Nature *576*, 465–470.

Johansson-Percival, A., He, B., Li, Z.J., Kjellen, A., Russell, K., Li, J., Larma, I., and Ganss, R. (2017). De novo induction of intratumoral lymphoid structures and vessel normalization enhances immunotherapy in resistant tumors. Nat. Immunol. *18*, 1207–1217.

Kim, D., Pertea, G., Trapnell, C., Pimentel, H., Kelley, R., and Salzberg, S.L. (2013). TopHat2: accurate alignment of transcriptomes in the presence of insertions, deletions and gene fusions. Genome Biol. *14*, R36.

Kvistborg, P., Philips, D., Kelderman, S., Hageman, L., Ottensmeier, C., Joseph-Pietras, D., Welters, M.J., van der Burg, S., Kapiteijn, E., Michielin, O., et al. (2014). Anti-CTLA-4 therapy broadens the melanoma-reactive CD8+ T cell response. Sci. Transl Med. *6*, 254ra128.

Larkin, J., Chiarion-Sileni, V., Gonzalez, R., Grob, J.J., Rutkowski, P., Lao, C.D., Cowey, C.L., Schadendorf, D., Wagstaff, J., Dummer, R., et al. (2019). Five-year survival with combined nivolumab and ipilimumab in advanced melanoma. N. Engl. J. Med. *381*, 1535–1546.

Li, B., and Dewey, C.N. (2011). RSEM: accurate transcript quantification from RNA-Seq data with or without a reference genome. BMC Bioinformatics *12*, 323.

Martinet, L., Filleron, T., Le Guellec, S., Rochaix, P., Garrido, I., and Girard, J.P. (2013). High endothelial venule blood vessels for tumor-infiltrating lymphocytes are associated with lymphotoxin beta-producing dendritic cells in human breast cancer. J. Immunol. *191*, 2001–2008.

Martinet, L., Garrido, I., Filleron, T., Le Guellec, S., Bellard, E., Fournie, J.J., Rochaix, P., and Girard, J.P. (2011). Human solid tumors contain high endothelial venules: association with T- and B-lymphocyte infiltration and favorable prognosis in breast cancer. Cancer Res. *71*, 5678–5687.

Martinet, L., Le Guellec, S., Filleron, T., Lamant, L., Meyer, N., Rochaix, P., Garrido, I., and Girard, J.P. (2012). High endothelial venules (HEVs) in human melanoma lesions: major gateways for tumor-infiltrating lymphocytes. OncoImmunology *1*, 829–839.

Menzies, A.M., Amaria, R.N., Rozeman, E.A., Huang, A.C., Tetzlaff, M.T., van de Wiel, B.A., Lo, S., Tarhini, A.A., Burton, E.M., Pennington, T.E., et al. (2021). Pathological response and survival with neoadjuvant therapy in melanoma: a pooled analysis from the International Neoadjuvant Melanoma Consortium (INMC). Nat. Med. *27*, 301–309.

Mikucki, M.E., Fisher, D.T., Matsuzaki, J., Skitzki, J.J., Gaulin, N.B., Muhitch, J.B., Ku, A.W., Frelinger, J.G., Odunsi, K., Gajewski, T.F., et al. (2015). Non-redundant requirement for CXCR3 signalling during tumoricidal T-cell trafficking across tumour vascular checkpoints. Nat. Commun. *6*, 7458.

Miller, B.C., Sen, D.R., Al Abosy, R., Bi, K., Virkud, Y.V., LaFleur, M.W., Yates, K.B., Lako, A., Felt, K., Naik, G.S., et al. (2019). Subsets of exhausted CD8(+) T cells differentially mediate tumor control and respond to checkpoint blockade. Nat. Immunol. *20*, 326–336.

Motz, G.T., Santoro, S.P., Wang, L.P., Garrabrant, T., Lastra, R.R., Hagemann, I.S., Lal, P., Feldman, M.D., Benencia, F., and Coukos, G. (2014). Tumor endothelium FasL establishes a selective immune barrier promoting tolerance in tumors. Nat. Med. *20*, 607–615.

Moussion, C., and Girard, J.P. (2011). Dendritic cells control lymphocyte entry to lymph nodes through high endothelial venules. Nature *479*, 542–546.

O'Sullivan, T., Saddawi-Konefka, R., Vermi, W., Koebel, C.M., Arthur, C., White, J.M., Uppaluri, R., Andrews, D.M., Ngiow, S.F., Teng, M.W., et al. (2012). Cancer immunoediting by the innate immune system in the absence of adaptive immunity. J. Exp. Med. *209*, 1869–1882.

Oliveira, G., Stromhaug, K., Klaeger, S., Kula, T., Frederick, D.T., Le, P.M., Forman, J., Huang, T., Li, S., Zhang, W., et al. (2021). Phenotype, specificity and avidity of antitumour CD8(+) T cells in melanoma. Nature *596*, 119–125.

Peng, D., Kryczek, I., Nagarsheth, N., Zhao, L., Wei, S., Wang, W., Sun, Y., Zhao, E., Vatan, L., Szeliga, W., et al. (2015). Epigenetic silencing of TH1-type chemokines shapes tumour immunity and immunotherapy. Nature *527*, 249–253.

Peske, J.D., Thompson, E.D., Gemta, L., Baylis, R.A., Fu, Y.X., and Engelhard, V.H. (2015). Effector lymphocyte-induced lymph node-like vasculature enables naive T-cell entry into tumours and enhanced anti-tumour immunity. Nat. Commun. *6*, 7114.

Petitprez, F., de Reynies, A., Keung, E.Z., Chen, T.W., Sun, C.M., Calderaro, J., Jeng, Y.M., Hsiao, L.P., Lacroix, L., Bougouin, A., et al. (2020). B cells are associated with survival and immunotherapy response in sarcoma. Nature *577*, 556–560.

Qiu, X., Hill, A., Packer, J., Lin, D., Ma, Y.A., and Trapnell, C. (2017). Single-cell mRNA quantification and differential analysis with Census. Nat. Methods *14*, 309–315.

Ribas, A., and Wolchok, J.D. (2018). Cancer immunotherapy using checkpoint blockade. Science *359*, 1350–1355.

Sade-Feldman, M., Yizhak, K., Bjorgaard, S.L., Ray, J.P., de Boer, C.G., Jenkins, R.W., Lieb, D.J., Chen, J.H., Frederick, D.T., Barzily-Rokni, M.,

et al. (2018). Defining T cell states associated with response to checkpoint immunotherapy in melanoma. Cell *175*, 998–1013.e1020.

Sharma, A., Subudhi, S.K., Blando, J., Scutti, J., Vence, L., Wargo, J., Allison, J.P., Ribas, A., and Sharma, P. (2019). Anti-CTLA-4 immunotherapy does not deplete FOXP3(+) regulatory T cells (Tregs) in human cancers. Clin. Cancer Res. *25*, 1233–1238.

Sharma, P., Siddiqui, B.A., Anandhan, S., Yadav, S.S., Subudhi, S.K., Gao, J., Goswami, S., and Allison, J.P. (2021). The next decade of immune checkpoint therapy. Cancer Discov. *11*, 838–857.

Siddiqui, I., Schaeuble, K., Chennupati, V., Fuertes Marraco, S.A., Calderon-Copete, S., Pais Ferreira, D., Carmona, S.J., Scarpellino, L., Gfeller, D., Pradervand, S., et al. (2019). Intratumoral Tcf1(+)PD-1(+)CD8(+) T cells with stem-like properties promote tumor control in response to vaccination and checkpoint blockade immunotherapy. Immunity *50*, 195–211 e110.

Spitzer, M.H., Carmi, Y., Reticker-Flynn, N.E., Kwek, S.S., Madhireddy, D., Martins, M.M., Gherardini, P.F., Prestwood, T.R., Chabon, J., Bendall, S.C., et al. (2017). Systemic immunity is required for effective cancer immunotherapy. Cell *168*, 487–502 e415.

Spranger, S., Dai, D., Horton, B., and Gajewski, T.F. (2017). Tumor-residing Batf3 dendritic cells are required for effector T cell trafficking and adoptive T cell therapy. Cancer Cell *31*, 711–723 e714.

Spranger, S., Spaapen, R.M., Zha, Y., Williams, J., Meng, Y., Ha, T.T., and Gajewski, T.F. (2013). Up-regulation of PD-L1, Ido, and T(regs) in the melanoma tumor microenvironment is driven by CD8(+) T cells. Sci. Transl Med. *5*, 200ra116.

Thiriot, A., Perdomo, C., Cheng, G., Novitzky-Basso, I., McArdle, S., Kishimoto, J.K., Barreiro, O., Mazo, I., Triboulet, R., Ley, K., et al. (2017). Differential DARC/ACKR1 expression distinguishes venular from non-venular endothelial cells in murine tissues. BMC Biol. *15*, 45.

Tumeh, P.C., Harview, C.L., Yearley, J.H., Shintaku, I.P., Taylor, E.J., Robert, L., Chmielowski, B., Spasic, M., Henry, G., Ciobanu, V., et al. (2014). PD-1 blockade induces responses by inhibiting adaptive immune resistance. Nature *515*, 568–571.

Veerman, K., Tardiveau, C., Martins, F., Coudert, J., and Girard, J.P. (2019). Single-cell analysis reveals heterogeneity of high endothelial venules and different regulation of genes controlling lymphocyte entry to lymph nodes. Cell Rep. *26*, 3116–3131.e3115.

von Andrian, U.H. (1996). Intravital microscopy of the peripheral lymph node microcirculation in mice. Microcirculation *3*, 287–300.

von Andrian, U.H., Thiriot, A., Farokhzad, O., and Shi, J. (2015). Endothelial cell genes and uses thereof. WIPO international patent application, WO2015/006500.

Wei, S.C., Anang, N.A.S., Sharma, R., Andrews, M.C., Reuben, A., Levine, J.H., Cogdill, A.P., Mancuso, J.J., Wargo, J.A., Pe'er, D., et al. (2019). Combination anti-CTLA-4 plus anti-PD-1 checkpoint blockade utilizes cellular mechanisms partially distinct from monotherapies. Proc. Natl. Acad. Sci. U S A *116*, 22699–22709.

Wei, S.C., Levine, J.H., Cogdill, A.P., Zhao, Y., Anang, N.A.S., Andrews, M.C., Sharma, P., Wang, J., Wargo, J.A., Pe'er, D., et al. (2017). Distinct cellular mechanisms underlie anti-CTLA-4 and anti-PD-1 checkpoint blockade. Cell *170*, 1120–1133.e1117.

Wingett, S.W., and Andrews, S. (2018). FastQ Screen: a tool for multi-genome mapping and quality control. F1000Res. *7*, 1338.

Wu, T.D., Madireddi, S., de Almeida, P.E., Banchereau, R., Chen, Y.J., Chitre, A.S., Chiang, E.Y., Iftikhar, H., O'Gorman, W.E., Au-Yeung, A., et al. (2020). Peripheral T cell expansion predicts tumour infiltration and clinical response. Nature *579*, 274–278.

Yost, K.E., Satpathy, A.T., Wells, D.K., Qi, Y., Wang, C., Kageyama, R., McNamara, K.L., Granja, J.M., Sarin, K.Y., Brown, R.A., et al. (2019). Clonal replacement of tumor-specific T cells following PD-1 blockade. Nat. Med. *25*, 1251–1259.

Please cite this article in press as: Asrir et al., Tumor-associated high endothelial venules mediate lymphocyte entry into tumors and predict response to PD-1 plus CTLA-4 combination immunotherapy, Cancer Cell (2022), https://doi.org/10.1016/j.ccell.2022.01.002

STAR★METHODS

KEY RESOURCES TABLE

REAGENT or RESOURCE	SOURCE	IDENTIFIER
Antibodies		
Rabbit polyclonal anti-Human/mouse CD31 unconjugated (Clone ab28364)	Abcam	Cat# ab28364; RRID: AB_726362
MECA-79 Rat IgM Hybridoma Supernatant	ATCC	Cat# ATCC HB-9479; RRID: CVCL_9222
Rat anti-Mouse B220 (Clone RA3-6B2)	BD Biosciences	Cat# 550286; RRID: AB_393581
Rat anti-Mouse CD8a (Clone 53-6.7)	BD Biosciences	Cat# 553027; RRID: AB_394565
Rat anti-Mouse CD31/PECAM1-APC (Clone MEC13.3)	BD Biosciences	Cat# 561814; RRID: AB_398497
Rat anti-Mouse CD62L-FITC (Clone MEL-14)	BD Biosciences	Cat# 553150; RRID: AB_394665
Rat anti-Mouse CD62L-PeCy7 (Clone MEL-14)	BD Biosciences	Cat# 560516; RRID: AB_1645257
Rat anti-mouse CD62P-Alexa Fluor 647 (Clone RB40.34)	BD Biosciences	Cat# 563674; RRID: AB_2738366
Rat anti-Mouse CD8a-APC (Clone 53-6.7)	BD Biosciences	Cat# 553035; RRID: AB_398527
Rat anti-Mouse CD45-BV711 (Clone 30-F11)	BD Biosciences	Cat# 563709; RRID: AB_2687455
Rat anti-Mouse CD62E biotin (Clone 10E9.6)	BD Biosciences	Cat# 553750; RRID: AB_395030
Rat anti-Mouse IFNγ-Alexa Fluor 647 (Clone XMG1.2)	BD Biosciences	Cat# 557735; RRID: AB_396843
Streptavidin-APC-Cy7	BD Biosciences	Cat# 554063; RRID: AB_10054651
Rat anti-Mouse CD3-APC-Cy7 (Clone 17A2)	BioLegend	Cat# 100222; RRID: AB_2242784
Anti-Mouse CD8a-Alexa Fluor 647 (Clone 53-6.7)	BioLegend	Cat# 100727; RRID: AB_493424
Anti-Mouse CD8a-Pacific Blue (Clone 53-6.7)	BioLegend	Cat# 100725; RRID: AB_493425
Rat anti-Mouse CD31/PECAM1-Pacific Blue (Clone 390)	BioLegend	Cat# 102422; RRID: AB_10613457
Anti-Mouse CD44-APC (Clone IM7)	BioLegend	Cat# 103012; RRID: AB_312963
Anti-Mouse CD44-BV605 (Clone IM7)	BioLegend	Cat# 103047; RRID: AB_2562451
Anti-Mouse CD44-APC-Cy7 (Clone IM7)	BioLegend	Cat# 103027; RRID: AB_830784
Anti-Mouse CD45 PerCP (Clone 30-F11)	BioLegend	Cat# 103130; RRID: AB_893339
Anti-Mouse Lymphotoxin beta Receptor (LTβR) (clone 5G11)	BioLegend	Cat# 134402; RRID: AB_1659177
Anti-Mouse PNAd-biotin (Clone MECA-79)	BioLegend	Cat# 120804; RRID: AB_493557
Anti-Mouse SLAMF6-PE (Clone 330-A5)	BioLegend	Cat# 134605; RRID: AB_1659258
Rat anti-Mouse TIM3-BV711 (Clone RMT3-23)	BioLegend	Cat# 119727; RRID: AB_2716208
Rat anti-Mouse PD-1-PeCy7 (Clone 29F.1A12)	BioLegend	Cat# 135215; RRID: AB_10696422
Rat anti-Mouse PD-L1-PeCy7 (Clone 10F.9G2)	BioLegend	Cat# 124313; RRID: AB_10643573
InVivoMAb anti-Mouse CD4 (clone GK1.5)	Bio X Cell	Cat# BE0003-1; RRID: AB_1107636
InVivoMAb anti-Mouse CD8a (clone 2.43)	Bio X Cell	Cat# BE0061; RRID: AB_1125541
InVivoMAb anti-Mouse CD62L (clone MEL-14)	Bio X Cell	Cat# BE0021; RRID: AB_1107665
InVivoMAb anti-Mouse CTLA-4 (clone 9D9)	Bio X Cell	Cat# BE0164; RRID: AB_10949609
InVivoMAb anti-Mouse PD-1 (clone RMP1-14)	Bio X Cell	Cat# BE0146; RRID: AB_10949053
InVivoMAb anti-Mouse PSGL-1 (clone 4RA10)	Bio X Cell	Cat# BE0186; RRID: AB_10950305
InVivoMAb rat IgG1 isotype control (clone HRPN)	Bio X Cell	Cat# BE0088; RRID: AB_1107775
InVivoMAb rat IgG2b isotype control (clone LTF-2)	Bio X Cell	Cat# BE0090; RRID: AB_1107780
InVivoMAb rat IgG2a isotype control (clone 2A3)	Bio X Cell	Cat# BE0089; RRID: AB_1107769
InVivoMAb mouse IgG2b isotype control (clone MPC-11)	Bio X Cell	Cat# BE0086; RRID: AB_1107791
Rabbit mAb anti-Human/Mouse TCF1- Alexa Fluor 488	Cell Signaling Technology	Cat# 6444S; RRID: AB_2797627
Rat anti-Mouse CD3-Alexa Fluor 700 (Clone 17A2)	eBioscience	Cat# 56-0032-80; RRID: AB_529508
Rat anti-Mouse CD3-eFluor 450 (Clone 17A2)	eBioscience	Cat# 48-0032-82; RRID: AB_1272193
Rat anti-Mouse CD4-FITC (Clone GK1.5)	eBioscience	Cat# 11-0041-85; RRID: AB_464893
Rat anti-Mouse CD4-PeCy7 (Clone GK1.5)	eBioscience	Cat# 25-0041-82; RRID: AB_469576
Rat anti-Mouse CD8a-PE (Clone 53-6.7)	eBioscience	Cat# 12-0081-83; RRID: AB_465531

(*Continued on next page*)

Please cite this article in press as: Asrir et al., Tumor-associated high endothelial venules mediate lymphocyte entry into tumors and predict response to PD-1 plus CTLA-4 combination immunotherapy, Cancer Cell (2022), https://doi.org/10.1016/j.ccell.2022.01.002

CellPress
OPEN ACCESS

Continued

REAGENT or RESOURCE	SOURCE	IDENTIFIER
Rat anti-Mouse CD31/PECAM1-eFluor 450 (Clone 390)	eBioscience	Cat# 48-0311-80; RRID: AB_10598808
Rat anti-Mouse CD45-APC (Clone 30-F11)	eBioscience	Cat# 17-0451-82; RRID: AB_469392
Rat anti-Mouse FoxP3-PE (Clone FJK-16s)	eBioscience	Cat# 12-5773-82; RRID: AB_465936
Rat anti-Mouse FoxP3-APC (Clone FJK-16s)	eBioscience	Cat# 17-5773-82; RRID: AB_469457
Syrian Hamster anti-Mouse gp38/Podoplanin-biotin (Clone eBio8.1.1)	eBioscience	Cat# 13-5381-82; RRID: AB_2016716
Syrian Hamster anti-Mouse gp38/Podoplanin-PeCy7 (Clone eBio8.1.1)	eBioscience	Cat# 25-5381-80; RRID: AB_2573459
Rat anti-Mouse Ki67-eFluor 660 (Clone SolA15)	eBioscience	Cat# 50-5698-82; RRID: AB_2574235
Rat anti-Human/Mouse High Endothelial Venule Marker-Alexa Fluor 488 (Clone MECA-79)	eBioscience	Cat# 53-6036-80; RRID: AB_10805867
Streptavidin-PeCy7	eBioscience	Cat# 25-4317-82; RRID: AB_10116480
Chicken anti-Goat IgG Alexa Fluor 647	Invitrogen	Cat# A21469; RRID: AB_1500603
Biotin Goat anti-Rat IgM μ chain specific	Jackson ImmunoResearch	Cat# 112-065-020; RRID: AB_2338171
Donkey anti-Goat IgG Alexa Fluor 488	Jackson ImmunoResearch	Cat# 705-545-147; RRID: AB_2336933
Donkey anti-Rabbit IgG Cy3	Jackson ImmunoResearch	Cat# 711-165-152; RRID: AB_2307443
Goat anti-Rat IgG Alexa Fluor 488	Jackson ImmunoResearch	Cat# 112-545-167; RRID: AB_2338362
Goat anti-Rat IgG Cy3	Jackson ImmunoResearch	Cat# 112-165-143; RRID: AB_2338250
Streptavidin Cy3	Jackson ImmunoResearch	Cat# 016-160-084; RRID: AB_2337244
Donkey anti-Rabbit IgG Biotin	Jackson ImmunoResearch	Cat# 711-065-152; RRID: AB_2340593
Donkey anti-Rat IgG Biotin	Jackson ImmunoResearch	Cat# 712-065-153; RRID: AB_2315779
Streptavidin-Alexa Fluor 488	Jackson ImmunoResearch	Cat# 016-540-084; RRID: AB_2337249
Goat anti-Mouse Ccl21-unconjugated	R&D Systems	Cat# AF457; RRID: AB_2072083
Anti-human CD8 rabbit monoclonal antibody (clone SP16)	Spring Bioscience	Cat# ab101500; RRID: AB_10710024
Biological samples		
Human metastatic melanoma biopsies (n=93). Unresectable stage III (n = 26) or IV (n = 67) metastatic melanoma treated with an anti-PD-1 antibody (nivolumab or pembrolizumab; i.v.), including twenty-eight in combination with an anti-CTLA-4 antibody (ipilimumab; i.v for 22 patients and i.t. in a distant metastasis for 6 patients). Patient samples are detailed in Table S3	MSN-08-027 CPP Ile de France	Registration number : 2008-A00373-52
Chemicals, peptides, and recombinant proteins		
MAXblock Blocking Medium	Active motif	Cat# 15252
BD Cytofix/Cytoperm™ Fixation/Permeablization Kit	BD Biosciences	Cat# 554714
OCT embedding matrix	CellPath	Cat # KMA-0100-00A
Collagenase IV	Gibco	Cat# KMA-0100-00A
CellTracker Deep Red Dye	Invitrogen	Cat# 17104-019
CellTrace CFSE Cell Proliferation Kit	Invitrogen	Cat# C34656
Calcein AM cell-permanent dye	Invitrogen	Cat# C34554
Qtracker 565 Vascular Labels	Invitrogen	Cat# Q21031MP
Fixable viability dye eFluor 506	Invitrogen	Cat# 65-0866-14
FoxP3/Transcription factor staining buffer set	Invitrogen	Cat# 00-5523-00
ACK lysing buffer	Lonza	Cat# 00-5523-00
RLT buffer	Qiagen	Cat# 79216
RNeasy Mini Kit	Qiagen	Cat# 10-548E
Collagenase VIII	Sigma	Cat# 74104

(*Continued on next page*)

Please cite this article in press as: Asrir et al., Tumor-associated high endothelial venules mediate lymphocyte entry into tumors and predict response to PD-1 plus CTLA-4 combination immunotherapy, Cancer Cell (2022), https://doi.org/10.1016/j.ccell.2022.01.002

Continued

REAGENT or RESOURCE	SOURCE	IDENTIFIER
DNaseI	Sigma	Cat# 74104
Fingolimod (FTY720)	Selleckchem	Cat# S5002
Cell Activation Cocktail (with Brefeldin A)	BioLegend	Cat # 423303
SuperScript VILO cDNA Synthesis Kit	ThermoFischer Scientific	Cat # 11754050
Power SYBR Green PCR Master Mix	ThermoFischer Scientific	Cat # 4368577
Critical commercial assays		
C1 Single-Cell Reagent Kit for mRNA Seq	Fluidigm	Cat# 100-6201
ArrayControl RNA Spikes	ThermoFisher	Cat# AM1780
SMARTer Ultra Low RNA Kit for the Fluidigm C1 System	Takara	Cat# 634833
Nextera XT kit	Illumina	Cat# FC-131-1096
High Sensitivity NGS Fragment Analysis kit	Agilent	Cat# DNF-474
EasySep™ Mouse T Cell Isolation Kit	StemCell	Cat# 19851
EasySep™ Mouse $CD4^+$ T Cell Isolation Kit	StemCell	Cat# 19852
Mouse CD8a + T Cell Isolation Kit	Miltenyi Biotec	Cat# 130-104-075
Mouse CD62L MicroBeads	Miltenyi Biotec	Cat# 130-049-701
Deposited data		
RNA-Seq data	This paper	GEO Series accession number - GEO: GSE154898
Mouse reference genome UCSC mm10	Genome Reference Consortium	https://genome.ucsc.edu/cgi-bin/hgGateway?db=mm10
Experimental models: Cell lines		
MCAreg (1969) fibrosarcoma	Diamond et al. (2011)	Gift from Robert Schreiber (Washington University School of Medicine, Saint-Louis, USA)
MCAprog (9609) fibrosarcoma	O'Sullivan et al. (2012)	Gift from Robert Schreiber (Washington University School of Medicine, Saint-Louis, USA)
MMTV-PyMT mammary carcinoma-derived VO-PyMT cells (PyMT)	Halpern et al. (2006)	Gift from Zena Werb (University of California, San Francisco, USA)
CT26 colon carcinoma cells	ATCC	Cat# ATCC CRL-2638
Experimental models: Organisms/strains		
Mouse: C57BL/6	Charles River	Cat# 027
Mouse: BALB/C	Charles River	Cat# 028
Mouse: FVB	Charles River	Cat# 207
Mouse: $Rag2^{-/-}$	House Breeding	
Oligonucleotides		
Primer: *Ackr1* Forward: AGGATGCTATGCTTGCCTGAA	This paper	
Primer: *Ackr1* Reverse: GGTGAAGCCACGGAGTTGA	This paper	
Primer: *Fut7* Forward: CAGATGCACCCTCTAGTACTCT	This paper	N/A
Primer: *Fut7* Reverse: TGCACTGTCCTTCCACAACC	This paper	N/A
Primer: *Glycam1* Forward: GTCCACTCCCACCAGCTACAC	This paper	N/A
Primer: *Glycam1* Reverse: GGCTCCTTGGAAAGGTCCTT	This paper	N/A
Primer: *Sele* Forward: TCCTGCGAAGAAGGATTTGAA	This paper	N/A
Primer: *Sele* Reverse: CCCCTCTTGGACCACACTGA	This paper	N/A
Primer: *Selp* Forward: CTCATCTGGTTCAGTGCTTTGATC	This paper	N/A
Primer: *Selp* Reverse: TCCACGCAGCCACTTCCT	This paper	N/A
Primer: *Hprt* Forward: CCTAAGATGAGCGCAAAGTTGAA	This paper	N/A
Primer: *Hprt* Reverse: CCACAGGACTAGAACACCTGCT	This paper	N/A

(*Continued on next page*)

Continued

REAGENT or RESOURCE	SOURCE	IDENTIFIER
Software and algorithms		
DiVa V8.0.1	BD Biosciences	
FlowJo v10.1	Tree Star	https://www.flowjo.com/
GraphPad Prism 8.2.1	GraphPad	www.graphpad.com
RSEM 1.2.18	Li and Dewey (2011)	https://github.com/deweylab/RSEM
Tophat2 2.0.14	Kim et al. (2013)	http://ccb.jhu.edu/software/tophat/index.shtml
Fastq Screen v0.9.5	Wingett and Andrews (2018)	https://github.com/StevenWingett/FastQ-Screen
FastQC 0.11.2		https://github.com/s-andrews/FastQC
Trimmomatic-32	Bolger et al. (2014)	https://github.com/genepattern/Trimmomatic
Monocle 2.0.4	Qiu et al. (2017)	https://github.com/cole-trapnell-lab/monocle-release
R 3.3.0 (packages: ggplot2 2.2.1; grid 3.3.2; gridExtra2.3; reshape2 1.4.3; scales 0.5.0; R package Monocle v2.4.0)		https://cran.r-project.org/bin/windows/base

RESOURCE AVAILABILITY

Lead contact

Further information and requests for resources and reagents should be directed to and will be fulfilled by the Lead Contact, Jean-Philippe Girard (Jean-Philippe.Girard@ipbs.fr).

Materials availability

The study did not generate new unique reagents.

Data and code availability

RNA-seq data have been deposited in NCBI's Gene Expression Omnibus and are accessible through GEO Series accession number GSE154898. All the other data supporting the findings of this study are available within the paper and its supplementary information files.

EXPERIMENTAL MODEL AND SUBJECT DETAILS

Patients

Ninety-three patients with unresectable stage III (n = 26) or IV (n = 67) metastatic melanoma were treated with an anti-PD-1 antibody (nivolumab or pembrolizumab; i.v.), including twenty-eight in combination with an anti-CTLA-4 antibody (ipilimumab; i.v for 22 patients and i.t. in a distant metastasis for 6 patients in the context of a phase II clinical trial, NCT02857569). The choice of the monotherapy versus the combination of ICB depends of various parameters : age and performance status of the patients, kinetics and aggressivity of the disease but also of the availability of the combination in terms of reimbursement at the time of treatment. Disease evaluation was determined using RECIST1.1 criteria (Eisenhauer et al., 2009): complete response (CR) and partial response (PR) for responders (R), or progressive disease (PD) and stable disease (SD) for non-responders (NR). The statistical comparison between responder and non-responder groups was performed using an unpaired two-sided Student's t-test. Overall survival was defined as the time interval from the date of ICB treatment initiation to the date of death or censoring from any cause. Progression-free survival (PFS) was defined as the time interval from the date of ICB treatment initiation to the date of developing radiographic progression, disease recurrence, death, or censoring from any cause. Overall survival and PFS were estimated using the Kaplan-Meier method and differences between groups assessed using the log-rank test. The analysis was done using R package survival. Patients received appropriate information and signed an informed consent form authorizing tumor biopsies and molecular studies in the context of an institutional CRB-approved protocol (MSN-08-027 CPP Ile de France, registration number: 2008-A00373-52). All tumors biopsies were collected before treatment and no other melanoma treatment was given between the date of the biopsy and the initiation of ICB treatment. Samples were immediately formalin-fixed and paraffin-embedded (FFPE) following tissue collection.

Mice

6-10-week-old female C57BL/6J, BALB/c and FVB wild-type mice were purchased from Charles River or Janvier. *Rag2*$^{-/-}$ mice on a C57BL/6 background (B6.129-Rag2^{tm1Fwa}) were obtained from European Mouse Mutant Archive (EMMA). All animals were

maintained in specific pathogen-free conditions with food and water provided *ad libitum*. Animals were housed 2 to 5 mice per cage. All mice were handled according to institutional guidelines under protocols approved by the French Ministry of Research and the FRBT (C2EA-01) animal care committee (Projects APAFIS#00664.02, APAFIS#12256-2017112021529157v3, APAFIS#12297-2017112313506769v2, APAFIS#23416-2019122019025727v3).

Cell lines

Methylcholanthrene (MCA) chemical carcinogen-induced tumor-derived MCA-progressor (MCA_{prog}) (9609) and MCA-regressor (MCA_{reg}) (1969) fibrosarcoma cells (Diamond et al., 2011; O'Sullivan et al., 2012) were obtained from Robert Schreiber (Washington University School of Medicine, Saint-Louis, USA). MMTV-PyMT mammary carcinoma-derived VO-PyMT cells (PyMT) (Halpern et al., 2006) and CT26 colon carcinoma cells (ATCC, CRL-2638), were obtained from Zena Werb (University of California, San Francisco, USA) and ATCC, respectively. MCA_{prog} and MCA_{reg} were cultured in RPMI 1640 (HyClone™, SH30096.01) with 10% Defined Fetal Bovine Serum, US origin (HyClone™, 30070.03), PyMT in DMEM (Gibco, 11960044) with 10% Fetal Bovine Serum (Gibco, 16250078), and CT26 in RPMI-1640 medium (ATCC, 30-2001) with 10% Fetal Bovine Serum (ATCC, 30-2021).

METHOD DETAILS

Tumor transplantation and tumor volume and weight measurements

MCA_{reg} (10^7 cells), MCA_{prog} (10^6 cells or 5×10^5 cells for ICB experiments and/or LTβR agonistic mAb), or CT26 (5×10^5 cells) tumor cells suspended in 100 μL DPBS, no calcium, no magnesium (Gibco, 14190094) were injected s.c. into the left flank of C57BL/6J (MCA_{prog} and MCA_{reg}) or BALB/c (CT26) mice. PyMT cells (5×10^5 cells in 100 μL DPBS) were injected s.c. in the area of the 4^{th} mammary gland fat-pad of FVB mice. Tumor growth was monitored by measuring the length and width of the tumors with calipers. The tumor volume was estimated using the formula: length × $width^2$ × 0.5, where length is the longest dimension and width is the corresponding perpendicular dimension. Tumor volume and tumor weight were measured on the indicated days. Changes in tumor size (length × width) after treatment were determined using the formula: (tumor size D12 – tumor size D9)/tumor size D9 × 100. Tumor regression, stabilization and progression were defined by > 10% decrease, < 10% change and > 10% increase, respectively.

In vivo treatments

Mice were treated i.p. with 200 μg of an anti-PD1 (RMP1-14, rat IgG2a, Bio X Cell) and/or 200 μg of an anti-CTLA-4 (9D9, mouse IgG2b, Bio X Cell) diluted in 200 μL DPBS, on days 3, 6 and 9 (for most experiments) or on days 6, 8 and 10 (for FTY720 and Block experiments). The mice were analyzed at day 12 post-tumor inoculation. In some experiments (triple therapy), ICB treatment with anti-PD1 and anti-CTLA-4 antibodies was combined with 10 μg of a LTβR agonistic mAb (5G11, rat IgG2a, Biolegend) injected i.t. on days 6, 8 and 10 in 50 μL DPBS, or with 40 μg of this LTβR agonistic mAb injected i.p. on days 3, 6 and 9 in 100 μL DPBS. Some triple therapy and dual ICB experiments were performed simultaneously with a single control experiment, as stated in the corresponding figure legends. In other experiments (monotherapy), mice were injected i.t. with 20 μg LTβR agonist mAb on day 6 and 10 μg on day 8, and the mice were analyzed at day 11 post-tumor inoculation. Rat IgG2a (clone 2A3, Bio X Cell) and mouse IgG2b (clone MPC-11, Bio X Cell) antibodies were used as isotype controls. To block lymphocyte trafficking during the course of ICB therapy, we injected mice i.p. with 30μg of FTY720 (Selleckchem) one day before the initiation of ICB treatment and every other day. FTY720 was also supplied in the drinking water (2,5 μg/mL) to maintain blockade. FTY720 was reconstituted in DMSO (50 mg/mL) and diluted in water. The ICB-treated group was injected with DMSO vehicle instead of FTY720. FTY720 efficacy was confirmed by measuring the reduction of $CD8^+$ T Cells in the blood. In another series of experiments (Block), mice were treated i.p. with function-blocking antibodies against L-selectin/CD62L (MEL-14, Bio X Cell) and PSGL-1 (4RA10, Bio X Cell) (200 μg/dose), starting one day before the initiation of ICB treatment. The ICB-treated group was injected with isotype controls instead of αCD62L/αPSGL-1 antibodies.

T cell depletion

Anti-Mouse CD4 (clone GK1.5, rat IgG2b, Bio X Cell) and anti-Mouse CD8a (clone 2.43, rat IgG2b, Bio X Cell) antibodies were used for *in vivo* depletion of $CD4^+$ and $CD8^+$ T cells, respectively. Control mice were treated with rat IgG2b isotype control (clone LTF-2, Bio X Cell). Antibodies (100 μg) were injected i.p. on days 1, 2, 3 and 6 and the mice were analyzed at day 12 post-tumor inoculation. $CD4^+$ and $CD8^+$ T cell depletion was confirmed by flow cytometry analysis of tumors and lymph nodes (LNs). For experiments with simultaneous ICB treatment and CD4 depletion, anti-Mouse CD4 antibodies or isotype controls were injected i.p. on days 1, 2, 3, 6 and 9. ICB treatment with anti-PD1 and anti-CTLA-4 antibodies was performed on days 3, 6 and 9.

Adoptive T cell transfer

$CD3^+$ T cells or $CD4^+$ T cells, isolated from the spleen of wild-type mice using EasySep™ Mouse T Cell Isolation Kit (StemCell # 19851) or EasySep™ Mouse $CD4^+$ T Cell Isolation Kit (StemCell # 19852), respectively, were adoptively transferred (5×10^6 cells) into recipient *Rag2*$^{-/-}$ mice before injection of MCA_{prog} tumor cells (10^6 cells, s.c.). Control mice were treated with PBS. Mice were analyzed at day 8 post-tumor inoculation.

Please cite this article in press as: Asrir et al., Tumor-associated high endothelial venules mediate lymphocyte entry into tumors and predict response to PD-1 plus CTLA-4 combination immunotherapy, Cancer Cell (2022), https://doi.org/10.1016/j.ccell.2022.01.002

CellPress
OPEN ACCESS

Preparation of single cell suspensions from tumors and lymph nodes

Tumors (MCA_{reg}, MCA_{prog}, CT26 or PyMT) and peripheral LNs (axillary, brachial, inguinal) were removed from mice using forceps, washed with digestion buffer (PBS with Ca^{2+} and Mg^{2+}, 2 % fetal bovine serum), and minced gently using scissors. In some experiments (endothelial cell sorting for RNA-seq and RT-qPCR analyses), tissues pieces were further dissociated using the flat end of a syringe plunger on 100 μM (tumors) or 40 μM (LNs) cell strainers, and washed with digestion buffer multiple times to eliminate some lymphocytes and enrich for stromal elements. Remaining tissue was placed in 1 mL (LNs) or 3 mL (tumors) digestion buffer with 1 mg/mL collagenase VIII (Sigma, C2139) and 10 μg/mL DNaseI (LNs) or 100 μg/mL DNaseI (tumors) for 25 min at 37°C on a rocker, and pipetted once to loosen tissue. Digestion was halted by adding digestion buffer with 5 mM EDTA and cells were filtered through a 100 μM cell strainer. Cells were then washed multiple times and resuspended in Staining Buffer (PBS, without Ca^{2+} and Mg^{2+}, 0.5% BSA, 2 mM EDTA).

Flow cytometry and cell sorting

Isolated cells from tumors or LNs were incubated with primary antibodies for 30 min, on ice in the dark, and then washed and resuspended in flow cytometry buffer (PBS without $Ca2^{+}$ and $Mg2^{+}$, 2% FBS, 5 mM EDTA). In some experiments, cells were washed after primary staining and subsequently incubated with streptavidin-conjugated antibodies for 15 min before washing and resuspension in flow cytometry buffer. For intracellular staining, cells were fixed and permeabilized using the Foxp3/Transcription Factor Staining Buffer Set (eBioscience), except for intracellular staining of IFNγ that was realized using Cytofix/Cytoperm kit (BD Biosciences), and stained according to manufacturer's protocol. Briefly, following cell surface staining, cells were fixed for 20 min at room temperature in the dark, then washed. Primary antibodies were incubated with cells in Fixation/Permeabilization buffer for 30 min; cells were then washed and resuspended in flow cytometry buffer. In some experiments, cells were washed after primary intracellular staining and subsequently incubated with secondary antibodies for 15 min before washing and resuspension in flow cytometry buffer. Samples were acquired on BD LSR II and Fortessa flow cytometers using DiVa software (BD Biosciences) and analyzed using FlowJo 10.1 (Tree Star). For cell sorting, a BD Influx was used. Starting cells were gated by FSC/SSC gates to select healthy, singlet populations. Endothelial cells were gated as $CD45^{-}CD31^{high}$ cells. The $CD31^{high}$ population was then further gated into MECA-79^{+} HECs (LN-HECs, iLN-HECs or TA-HECs for homeostatic LNs, inflamed LNs or tumors, respectively) and MECA-79^{-} ECs (LN-ECs or TA-ECs, for LNs or tumors, respectively). Tumor-infiltrating exhausted $CD8^{+}$ T cells were gated as $CD44^{+}PD\text{-}1^{+}CD8^{+}$ T cells and then further gated into $SLAMF6^{+}TIM\text{-}3^{-}$ (stem-like) and $SLAMF6^{-}TIM\text{-}3^{+}$ (terminally exhausted) subsets. SLAMF6 (Ly108) is considered a reliable surface marker for $PD\text{-}1^{+}TCF\text{-}1^{+}$ stem-like $CD8^{+}$ T cells (Miller et al., 2019). Stem-like phenotype of $SLAMF6^{+}TIM\text{-}3^{-}CD44^{+}PD\text{-}1^{+}CD8^{+}$ T cells was verified by intracellular staining for TCF1. $SLAMF6^{+}TIM3^{-}$ cells expressed high levels of TCF-1 and intermediate levels of PD-1, and $SLAMF6^{-}TIM3^{+}$ cells expressed higher levels of PD-1 (Figure S4I). $CD8^{+}/T_{regs}$ and $CD4^{+}/T_{regs}$ ratios were calculated with cells per mg tumor. For *ex vivo* analysis of IFNγ production by tumor-infiltrating T cells, cells were stimulated with a PMA/Ionomycin cocktail containing Brefeldin A at 1/500 dilution (Biolegend, 423303) and incubated for 4h at 37 °C. $CD4^{+}$ and $CD8^{+}$ T cells were then analyzed by flow cytometry.

The following antibodies and reagents were used: CD62L-FITC (MEL-14, BD Biosciences), CD62L-PeCy7 (MEL-14, BD Biosciences), CD44-BV605 (IM7, BioLegend), CD44-APC (IM7, BioLegend), CD44-APC-Cy7 (IM7, BioLegend), CD45-BV711 (30F-11, BD Biosciences), CD45-APC (30-F11, eBioscience), CD45-PerCP (30-F11, BioLegend), CD3-Alexa Fluor 700 (17A2, eBioscience), CD3-eFluor450 (17A2, eBioscience), CD3-APC-Cy7 (17A2, BioLegend), CD8a-APC (53-6.7, BD Biosciences), CD8a-Alexa Fluor 647 (53-6.7, BioLegend), CD8a-PE (53-6.7, eBioscience), CD8a-PB (53-6.7, BioLegend), CD4-FITC (GK1.5, eBioscience), CD4-PeCy7 (GK1.5, eBioscience), FoxP3-PE (FJK-16s, eBioscience), FoxP3-APC (FJK-16s, eBioscience), Ki67-eFluor 660 (Clone SolA15, eBioscience), PD-1-PeCy7 (29F.1A12, BioLegend), SLAMF6-PE (330-A5, BioLegend), TIM3-BV711 (RMT3-23, BioLegend), TCF1-AF488 (C63D9, Cell Signaling Technology), CD31/PECAM1-e450 (Clone 390, eBioscience), CD31-APC (MEC13.3, BD Biosciences), CD31-PB (390, BioLegend), PNAd-Biotin (MECA-79, BioLegend), Anti-Human/Mouse High Endothelial Venule Marker-Alexa Fluor 488 (Clone MECA-79, eBioscience), gp38/Podoplanin-biotin (eBio8.1.1, eBioscience), gp38/Podoplanin-PeCy7 (eBio8.1.1, eBioscience), PD-L1-PeCy7 (10F.9G2, BioLegend), IFNγ-Alexa Fluor 647 (XMG1.2, BD Biosciences), CD62P-Alexa Fluor 647 (RB40.34, BD Biosciences), Goat anti-mouse CCL21 unconjugated (AF457, R&D Systems), Streptavidin-APC-Cy7 (BD Biosciences), Streptavidin-PeCy7 (eBioscience), Chicken anti-Goat Alexa Fluor 647 (Invitrogen) and Fixable viability dye eFluor 506 (Invitrogen).

Immunofluorescence staining of mouse tissues

Tumors or LNs removed from mice using forceps were fixed in paraformaldehyde 4% 6h at 4°C or 1h at room temperature and incubated overnight in 30% sucrose solution (DPBS). Samples were either flash frozen in OCT embedding media using liquid nitrogen or, embedded in paraffin using an Excelsior AS Tissue Processor. Formalin-fixed paraffin-embedded (FFPE) sections were cut at 5 μm, deparaffinized and rehydrated. Epitope retrieval was performed using citrate buffer pH 6.0 using a microwave for 15 min. Frozen samples were cut at 5–10 μm using a Cryostat (Leica) and allowed to dry. Both FFPE and cryostat sections were washed with PBS, incubated with MAXblock Blocking Medium (Active Motif, 15252) for 1 h, and then stained with primary antibodies overnight at 4°C in PBS + 20% MAXblock. The following antibodies were used: Rat anti-Human/Mouse High Endothelial Venule Marker-Alexa Fluor 488 (Clone MECA-79, eBioscience), Rabbit polyclonal Anti-Human/Mouse CD31 unconjugated (Clone ab28364, Abcam), Rat anti-mouse CD8a (clone 53-6.7, BD Biosciences), Rat Anti-Mouse B220 (clone RA3-6B2, BD Biosciences), Goat anti-mouse CCL21 unconjugated (Clone AF457, R&D Systems), Rat Anti-Mouse CD62E/E-selectin biotin (Clone 10E9.6, BD Pharmingen). All secondary antibodies (Donkey anti-goat IgG-AF488, ref 705-545-147; Goat anti-rat IgG-AF488, ref 112-545-049; Goat anti-rat

IgG-Cy3, ref 112-165-049; Donkey anti-rabbit IgG-Cy3 ref 711-165-152; Donkey anti-rabbit IgG-Biotin, ref 711-065-152; Donkey anti-rat IgG-Biotin, ref 712-065-153), Streptavidin-Cy3 (ref 016-160-084) and Streptavidin-Alexa Fluor 488 (ref 016-540-084) were purchased from Jackson ImmunoResearch, excepted Chicken anti-goat IgG-AF647 (Invitrogen, A21469). Slides were washed 3 times for 3 min and then incubated with secondary antibodies in PBS + 20% MAXblock for 1 h. Slides were washed 3 times, incubated with DAPI for 5 min, then washed and mounted in Mowiol. Low-magnification photos were taken using a Zeiss wide-field microscope and high-magnification photos were taken using an Olympus confocal microscope. ImageJ was used for processing microscopy images.

Immunohistochemistry of human melanoma samples

CD8 immunohistochemistry was performed using a Ventana Discovery Ultra platform. After deparaffinization, epitope retrieval was performed for 32 min in CC1 buffer (Tris-EDTA based buffer pH 7.8). The primary anti-CD8 rabbit monoclonal antibody (clone SP16, Spring Bioscience) was incubated for 1 h at 37 °C. An anti-rabbit Ultra-MAP kit coupled to HRP and a purple chromogen were used for detection. $CD8^+$ T cells densities were determined by counting $CD8^+$ cells on 10 high-power field (10 HPF) of view ($\sim 2\ mm^2$). Counting was performed by two independent pathologists (IM, JYS), who were blind to the clinical outcome.

For detection of MECA-79^+ TA-HEVs, sections were first deparaffinized and rehydrated using Leica ST5010 Autostainer XL machine. Epitope retrieval was performed using citrate buffer pH 6.0 using a microwave for 3 × 5 minutes at 700Watts. Endogenous peroxidase activity was blocked in methanol/H2O2 0.3% solution for 30 min. Sections were equilibrated with PBS, incubated with MAXblock Blocking Medium (15252, Active Motif) for 1 h, and then incubated with MECA-79 mAb supernatant overnight at 4°C. Then the following antibodies were used: biotin goat anti-rat IgM, μ chain specific (Ref 112-065-020, Jackson ImmunoResearch) and peroxidase-conjugated streptavidin (Ref: 016-030-084, Jackson ImmunoResearch). Staining was revealed with 3,3′-Diaminobenzidine tablets (D4293, Sigma). Sections were counterstained with Gill hematoxylin (ref H-3401, Vector) and mounted with mounting media (ref: MMC0226 CoverSafe). Tumor slides stained with MECA-79 were scanned using a high-resolution scanner (Nanozoomer HT automated slide scanner). The numbers of MECA-79^+ TA-HEVs in the melanoma lesions were scored by three independent observers (JC, NO, JPG), who were blind to the clinical outcome, using a four-grade scale (score 0, 1, 2, 3 for absent, low, moderate and high numbers of MECA-79^+ TA-HEVs). A consensus was reached in cases of disagreement. When two different samples were available (7 patients out of 93), the TA-HEV scores in lymph node or skin metastases (rather than in other metastatic sites) were used for the statistical analyses. Lesions containing high or moderate numbers of TA-HEVs (TA-HEV scores 3 or 2) were defined as TA-HEV^{high} lesions; lesions containing low numbers of TA-HEVs (TA-HEV scores 1 or 0) were defined as TA-HEV^{low} lesions.

Real-time qPCR (RT-qPCR)

TA-HECs and TA-ECs from MCA_{reg} or MCA_{prog} tumors pooled from 3 mice, and LN-HECs and LN-ECs from peripheral LNs pooled from 3 mice, were sorted on a BD influx into low binding tubes containing 350 μL of RLT Buffer (QIAGEN, 74104) supplemented with 1% β-mercaptoethanol. Total RNA was isolated using an RNeasy Mini Kit (QIAGEN, 74104) and cDNA were synthesized using SuperScript" VILO cDNA Synthesis Kit according to the manufacturer's instructions (ThermoFisher Scientific, 11754-050). qPCR was performed using the ABI7500 Prism SDS Real-Time PCR Detection System (Applied Biosystems) with Power SYBR Green PCR Master Mix (ThermoFisher Scientific, 4367659) and a standard temperature protocol. The results are expressed as relative quantities and calculated using the 2-ΔΔCT method. Genes were analyzed in triplicate, and two to four separate qPCR experiments were performed for each gene. Primers were designed using Primer Express software and were purchased from Sigma-Aldrich. *Hprt* was used as a control gene for normalization.

Short-term homing assays

Homing assays were performed 7 days after injection of tumor cells in recipient mice. Single cell suspensions of lymphocytes (comprising $CD4^+$ T cells, $CD8^+$ T cells and B cells) were prepared from the spleen of tumor-bearing mice or naive mice (after lysis of red blood cells in ACK lysing buffer, Lonza 10-548E), counted, labeled with CellTracker CFSE Dye (Invitrogen, C34554) or CellTracker Deep Red Dye (Invitrogen, C34656), and injected (20×10^6 cells) into the tail vein of tumor-bearing mice. After 1 h, mice were sacrificed and both tumors and inguinal lymph nodes were isolated. The phenotype of labeled T cells ($CD45^+CD3^+CFSE^+$ or $CD45^+CD3^+DeepRed^+$) recruited into tumors and lymph nodes was analyzed by flow cytometry. Although homing assays were performed in both MCA_{reg} and MCA_{prog} tumors models, the MCA_{prog} model (MCA_{prog}, 10^6 cells injected) was selected for phenotypic analyses because these analyses were more technically challenging in the MCA_{reg} model, due to the small size of these regressing tumors.

For comparison of lymphocyte homing in MCA_{prog} tumors with or without ICB treatment, single cell suspensions of lymphocytes (comprising $CD4^+$ T cells, $CD8^+$ T cells and B cells) were prepared from the spleen and lymph nodes of tumor-bearing mice, labeled with CellTracker Deep Red Dye (Invitrogen, C34656), and injected (20×10^6 cells) into the tail vein of tumor-bearing mice, not treated or treated with ICB (analysis at day 12). After 1 h, mice were sacrificed, tumors were isolated, and the number of fluorescent lymphocytes (Deep Red^+ cells) recruited into tumors was analyzed by flow cytometry. Results are expressed as relative homing ratio (mean ± SEM) which was calculated by dividing the number of Deep Red^+ cells per mg of tumor (for each individual mouse treated with isotype control mAb or ICB) with the mean number of Deep Red^+ cells per mg of tumor after isotype control mAb treatment. Hence, homing ratio = 1 represents lymphocyte homing to tumor after isotype control mAb treatment. The ratios of the number of Deep Red^+ cells per mg of tumor divided by the number of TA-HECs per mg of tumor were also determined for each individual mouse.

Please cite this article in press as: Asrir et al., Tumor-associated high endothelial venules mediate lymphocyte entry into tumors and predict response to PD-1 plus CTLA-4 combination immunotherapy, Cancer Cell (2022), https://doi.org/10.1016/j.ccell.2022.01.002

CellPress
OPEN ACCESS

Wide-field intravital microscopy

Mice were anesthetized by i.p. injection of 1 mg/ml of xylazine and 5 mg/ml of ketamine per kg/mouse and placed on a customized stage for immobilizing the tumor and securing the animals. A heating pad with temperature feedback to an mTCII microTemperature Controller (Cell MicroControls, Norflok, VA, USA) assured a constant temperature for the mouse. The right femoral artery was catheterized for retrograde injection of labeled cells, and subcutaneous tumor was exposed for intravital microscopy as previously described for lymph node (Moussion and Girard, 2011; von Andrian, 1996). Mouse was then transferred to a customized intravital video microscopy setup (INM100, Leica Microsystems SA, Rueil-malmaison, France) equipped with water immersion objectives (HCX APO; Leica Microsystems). Single cell suspensions of lymphocytes (comprising $CD4^+$ T cells, $CD8^+$ T cells and B cells) were isolated from the spleen of tumor-bearing mice (treated or not with ICB) or naive mice, after lysis of red blood cells in ACK lysing buffer (Lonza), labeled with calcein AM (C3100MP, Invitrogen) for 5 minutes at 37°C (1 μg calcein AM/10^7 cells/100 μl physiological serum), and injected into the right femoral artery of tumor-bearing mice (treated or not with ICB). In some experiments, lymphocytes isolated from the spleen and lymph nodes of MCAprog tumor-bearing mice treated with dual ICB, enriched for $CD8^+$ T cells (mouse CD8a + T Cell Isolation Kit, Miltenyi Biotec) and depleted of $CD62L^+$ cells (mouse CD62L MicroBeads, Miltenyi Biotec), were used for intravital microscopy analysis of the behavior of $CD62L^-$ cells (> 98% $CD62L^-$ cells) within TA-HEVs. Fluorescent events in the tumor microcirculation were visualized and recorded by an EB-CCD camera (Hamamatsu Photonics, Massy, France) at different positions of the tumor and stored on DVCAM video tapes (DSR-11 Sony, IEC-ASV, Toulouse, France). At the end of the experiment, non-blocking amounts of fluorescent MECA-79 mAb (Alexa Fluor-488-labeled MECA-79 mAb; 10–20 μg; eBioscience 53-6036-82) was injected intravenously in retro-orbital to identify $MECA\text{-}79^+$ TA-HEVs in the tumor microcirculation. In some experiments, the tumor microvasculature and $MECA\text{-}79^+$ TA-HEVs were visualized using both intravital INM100 microscope and MacroFluo (Leica). Rolling fractions (the percentage of rolling cells in the total flux of cells in each blood vessel) and sticking fractions (the percentage of rolling cells that firmly adhered for a minimum of 30 seconds) were calculated off-line for $MECA\text{-}79^+$ and $MECA\text{-}79^-$ blood vessels. When indicated, cells were pretreated for 30 min with function-blocking antibodies against L-selectin (MEL-14, Bio X Cell) and PSGL-1 (4RA10, Bio X Cell) (100 μg/10^8 cells).

Multiphoton *in vivo* imaging

Mice were prepared as described above for wide-field intravital microscopy for tumor immobilization and exposition, and maintained under anesthesia with isofluran inhalation during the whole multiphoton imaging session. Non-blocking amounts of Alexa Fluor 488-labeled MECA-79 mAb (10–20 μg) were injected i.v. and tumors were imaged by wide-field intravital microscopy at the begining and at the end of the multiphoton imaging experiments in order to visualize and localize $MECA\text{-}79^+$ TA-HEVs in the tumor microcirculation. Calcein AM-labeled single cell suspensions of lymphocytes (comprising $CD4^+$ T cells, $CD8^+$ T cells and B cells) isolated from the spleen of tumor-bearing mice treated with ICB (after lysis of red blood cells in ACK lysing buffer) were then injected into the right femoral artery of tumor-bearing mice treated with ICB, and fluorescent events in $MECA\text{-}79^+$ TA-HEVs were acquired by multiphoton imaging on a 7MP upright microscope (Carl Zeiss, Jena, Germany) equipped with a |×20×| objective. Blood vessels were visualized with 20 μL of a Qtracker-565 (2μM, Q21031MP Invitrogen). Excitation was provided by a Ti-Sapphire femtosecond laser, Chameleon Ultra 2 (Coherent Inc.) tuned at 800 nm and emitted fluorescence was collected with 2 non-descanned detectors: Channel 1 (500–550 nm) for calcein-labeled lymphocytes and Channel 2 (565–610 nm) for blood vessels. For time analysis of cells migration in $MECA\text{-}79^+$ TA-HEVs, stacks of 33 to 68 slices (XY from 204*212 to 460*463μm) were acquired every 60 or 90s (DZ = 5μm). Offline, stacks were aligned and maximum intensity projection performed with Imaris (Bitplane, Zurich, Switzerland) to obtain a top view of cells behavior and create movies.

Transcriptome profiling by RNA sequencing

Full length RNA-seq

The Fluidigm C1 System was used to prepare full-length cDNA libraries and perform RNA-sequencing (RNA-seq). After preparation of single cell suspensions from $TA\text{-}HEV^{high}$ MCA_{reg} tumors (10^7 tumor cells injected at day 0; RNA-seq analysis at day 7), homeostatic lymph nodes or inflamed lymph nodes (immune-stimulation by skin painting with 4% oxazolone; RNA-seq analysis at day 3) (Veerman et al., 2019), fluorescent antibody-labeled cells were sorted on a BD Influx into low-binding tubes containing 3 μL of staining buffer. Cells were then counted using a hemocytometer and placed into the C1 chip at a 7:3 ratio (7 μL of cell suspension at 66,000–333,000 cells/mL, mixed with 3 μL of Suspension Reagent) according to manufacturer instructions (Fluidigm). 5 μL were then injected into the chip, ensuring that a total of 230–1165 cells were loaded on the C1 chip. HECs were captured using a 10–17 μm chip and ECs were captured using a 5–10 μm chip according to manufacturer's instructions (Fluidigm C1 System Software v1.5 and v2.1.2). After loading, photos of each capture site were taken using a Zeiss wide-field microscope for further analysis. Thermo Fisher ArrayControl RNA Spikes (Cat # AM1780) were added to the lysis mix for quality control as per the SMARTer protocol. Reverse transcription of mRNA and synthesis of whole transcriptome full-length amplified complementary DNA (cDNA) by template switching were performed on the C1 chip using the SMARTer Ultra Low RNA Kit for the Fluidigm C1 System (Takara). Amplified cDNA from the C1 was verified using a Fragment Analyzer (Agilent DNF-474_HS NGS Fragment Analysis Kit 1bp-6000bp). cDNA samples containing sufficient amounts of cDNA (> 0.1 ng/ml, as determined by the Agilent Fragment Analyzer) and no contaminating cells (capture sites were photographed using a wide-field fluorescence microscope and sites containing contaminating cells expressing either CD45 or gp38 coupled with PE were discarded from further processing) were used to generate cDNA libraries using the Nextera XT DNA Library Preparation Kit as per the manufacturer's instructions (Illumina). After tagmentation, PCR amplification

and cleaning, libraries were pooled and paired-end sequencing was performed using a Illumina HiSeq3000 sequencer to a sequencing depth > 2 million reads/single cell.

RNA-seq data processing and quality control

Paired-end reads were trimmed using trimmomatic-0.32 (Bolger et al., 2014) using the parameters: (ILLUMINACLIP:$(adapters): 2:30:10 LEADING:3 TRAILING:3 SLIDINGWINDOW:4:15 MINLEN:36). It removed Nextera adapters from read ends, removed low quality bases from edges and removed any reads that were shorter than 36 reads. Trimmed reads were then aligned to the UCSC mm10 mouse genome using RSEM v1.2.18 (Li and Dewey, 2011) with default settings. The gtf file of mm10 was slightly modified to remove *Ccl21a* pseudogenes (*Gm1987*, *Gm10591*, *Gm13304*, and *Gm21541*) as multiple mapping caused reads to be discarded. Gene expression values were calculated as Fragments Per Kilobase of transcript per Million (FPKM) and were obtained from resulting RSEM output.

To filter low quality sequences and cells, fractions of reads mapping to the mouse genome, spike-in controls and mitochondrial genes were calculated for each cell. To filter low quality samples, FASTQ files were first analyzed using fastqscreen v0.9.5 (Wingett and Andrews, 2018) for non-murine contaminants. Then FASTQC v0.11.2 was run on samples before and after trimming to evaluate quality of reads and adaptor contamination. TopHat2 v2.0.14 (Kim et al., 2013) was used to measure the percentage of reads that aligned to RNA spike-ins or mitochondrial genes using fasta files containing either 3 Ambion Spike-In controls or the murine mitochondrial genome (mm10). The option–no discordant was applied to tophat2. We removed any samples where reads aligned more than 20% RNA to spike-in controls or more than 15% to mitochondrial genes (Veerman et al., 2019). We also verified whether cells expressed distinct cell markers associated with other cell types such as lymphocytes and discarded any samples with high expression. Only data from high-quality cells with > 3000 genes detected per cell, were used for further analysis.

Bioinformatic analysis of differential gene expression

Bioinformatic analysis of the RNA-seq data was performed using R 3.3.0 software. We used the R package Monocle v2.4.0 (Qiu et al., 2017) to define differentially expressed genes between individual conditions using FPKM with a lowerDetectionLimit = 0.01, expressionFamily = tobit and minimum expression of 5 cells. We added an arbitrary cell to each condition, which contained an FPKM of 1.1 of each gene, allowing comparisons of genes expressed in one condition but not in another. Monocle normalized expression values to account for technical variation in RNA recovery and sequencing depth. Statistically significant differentially expressed genes were identified using Monocle which provided p values and adjusted p values (q = multiple testing corrected p values) of each data set. $q < 0.05$ was considered to be significant and $q > 0.05$ was considered to be non-significant. Graphics were made using the R core package and packages ggplot2 2.2.1, grid 3.3.2, gridExtra 2.3, reshape2 1.4.3, and scales 0.5.0.

QUANTIFICATION AND STATISTICAL ANALYSIS

Prism 8.2.1 software (GraphPad) was used to perform statistical analyses and to create bar graphs and dot plots of flow cytometry, tumor growth, RT-qPCR and intravital microscopy data. Statistics for flow cytometry, cell counts and RT-qPCR data, tumor weights, HEV diameters and HEV scores were determined by unpaired two-tailed Student's t tests or by two-tailed Mann-Whitney tests. Statistics for intravital microscopy data (rolling fractions, sticking fractions) were determined by two-tailed Mann-Whitney tests. For experiments containing more than two groups (depletion of $CD4^+$ and $CD8^+$ cells, ICB monotherapies and dual ICB with FTY720), a one-way ANOVA with Tukey's multiple comparison test or a Kruskal Wallis with Dunn's multiple comparaison test were performed. Differences were considered statistically significant when $P < 0.05$.